The Dissertation Committee for Xinyu Li Certifies that this is the approved version of the following dissertation:

Computational investigation of functional perovskites

Committee:

Graeme A. Henkelman, Supervisor

Jianshi Zhou, Co-Supervisor

John B. Goodenough

Gyeong S. Hwang

Computational investigation of functional perovskites

by

Xinyu Li

Dissertation

Presented to the Faculty of the Graduate School of

The University of Texas at Austin

in Partial Fulfillment

of the Requirements

for the Degree of

Doctor of Philosophy

The University of Texas at Austin

May 2018

Dedicated to my family.

Acknowledgements

I sincerely thank my advisors, Graeme Henkelman, Jianshi Zhou and Nicole Benedek, for their inspiring guidance on my graduate study. I also thank my parents, Ying and Lanrong, for their support during my education and my wife, Xuemin, for her encouragement and accompaniment.

I benefit a lot from my group members and collaborators. I thank Penghao Xiao, Zhiyao Duan, Lei Li, Hao Li and Wenrui Chai for their helpful discussion on computational theories and tools. I will also thank Zongyao Li, Xiang Li and Xi Chen for their guidance on experimental techniques.

Computational investigation of functional perovskites

Publication No._____

Xinyu Li, Ph.D.

The University of Texas at Austin, 2018

Supervisor: Graeme A. Henkelman

Co-supervisor: Jianshi Zhou

Functional perovskites have been investigated extensively for many years. Thousands of new perovskites are synthesized and studied every year. Many functional perovskites have been widely employed in industry. Density functional theory (DFT) calculations have been used to obtain a better understanding of functional perovskites, especially their electronic and structural properties. During my graduate study, I investigated perovskite's properties on ionic transport, magnetic ordering, ferroelectricity, physical property and phase transition using DFT calculations.

In the first case, I simulated the ionic transport process in several Ruddlesden-Popper (RP) phases. Climbing image nudged elastic band (CI-NEB) calculation was used to get accurate oxygen interstitial migration barrier. I established a linkage between interstitial migration barrier and perovskite's octahedral rotation with symmetry mode approach. Two factors, including A-site atom radius and epitaxial strain, were used to reduce interstitial migration barrier in my simulation. My study on ionic transport in RP phases provides guidance on the design of fast ionic transport in perovskite oxides.

In the second case, DFT calculation was employed to investigate a double perovskite's magnetic and electronic properties. A new ferroelectric mechanism in perovskite, associated with the displacement of coplanar Mn^{2+}, was discovered experimentally. My DFT calculation explained the origin of coplanar displacement from an orbital point of view. In addition, DFT simulations were used in the design of ferroelectricity enhancement perovskite.

In the last case, I simulated structural behaviors under pressure of several double perovskites. The results show that these double perovskites can be divided into two groups based on their octahedral rotations under pressure. The origin of their distinct volume reduction mechanisms was studied through DFT simulations. The difference between the two mechanisms and their influence on bulk modulus were discussed based on my computational results.

Table of Contents

List of Figures

List of Tables

Chapter 1

Introduction

This dissertation is a collection of works I completed during my Ph.D. study in the materials science and engineering program at The University of Texas at Austin. My studies primarily focus on the employment of computational tools for the investigation of functional perovskites. Functional perovskites have received extensive study due to their various applications. New theories and materials are rapidly emerging with the help of more powerful experimental technologies. At the same time, the development of computational theories and supercomputers provides a practical tool in the investigation of perovskite's fundamental science. In this dissertation, I present several computational studies in the exploration of the fundamental science of functional perovskites.

Each chapter presents a self-contained study of functional perovskite research. The first chapter focuses on the understanding of oxide ion transport mechanism and ways to enhance ionic transport in Ruddlesden-Pepper phases, which serve as cathodes in solid oxide fuel cells. The second chapter focuses on the exploration of ferroelectricity mechanism in the double perovskite $CaMnTi_2O_6$ and the design of similar double perovskites with larger dipole moment. The third chapter discusses a bulk modulus study of $CaCu_3M_4O_{12}$ perovskites. Two volume reduction mechanisms were discovered under external pressure. An association between Γ_2^+ octahedral rotation and the selection on volume reduction mechanism is established through symmetry-mode approach.

1.1 Perovskite and perovskite structure

Perovskite oxides have been extensively studied and widely employed in industry since their discovery in 1839. Various perovskite-related oxides have shown their applications in green energy,[1-2] superconductivity, metal-insulator transitions, magnetism, ferroelectricity and many other fields. For example, $La_2NiO_{4+\delta}$ has been employed as an electrode material in solid oxide fuel cells.[3-4] Perovskite $CH_3NH_3PbI_{3-x}Cl_x$ has been proved a promising material for solar cell due to its high photovoltaic efficiency.[5] $Ba_{1-x}K_xBiO_{3-y}$ shows superconductivity at around 30K.[6] Double perovskite Sr_2YIrO_6 has been synthesized and shown novel magnetism on Ir^{5+} ions.[7] Doping and oxygen vacancy are producing more and more perovskite ferroelectric materials.[8-9]

A typical perovskite has a chemical formula of $A^{3+}B^{3+}X_3^{2-}$, $A^{2+}B^{4+}X_3^{2-}$ and $A^{1+}B^{5+}X_3^{2-}$.[10-11] Most metallic elements can be either an A or a B-site atom, while X atoms are usually oxygen and sulfur.[12] Each A-site atom is surrounded by 12 X-site atoms and B-site atoms stay within the octahedron made of six X-site atoms. All BX_6 octahedra are corner-shared, producing a three-dimensional octahedral network. The large number of A and B-site candidate atoms makes A-O and B-O bond lengths vary in a wide range. A tolerance factor t (equation 1.1) is used to measure the mismatch between the A-O and B-O bond lengths. When tolerance factor equals to one, A-O and B-O bond lengths are perfectly matched in the cubic structure. A tolerance factor smaller than one requires cooperative rotations of the BX_6 octahedra, which lowers the symmetry of perovskite structure.

Layered perovskites are an important family of perovskite materials. Different from the three-dimensional octahedral network in perovskites, layered perovskites are made of BX_6 octahedral layers, separated by A and X-site atoms,

shown in Figure 1.1. Based on the arrangement of BX_6 octahedral layers and interlayer atoms, layered perovskites are separated into three phases: Aurivillius phase, Dion-Jacobson phase and Ruddlesden-Popper phase. The variety of ions and complex configuration of the octahedral network provide people powerful tools to manipulate perovskite's properties, which makes perovskites attractive functional materials.

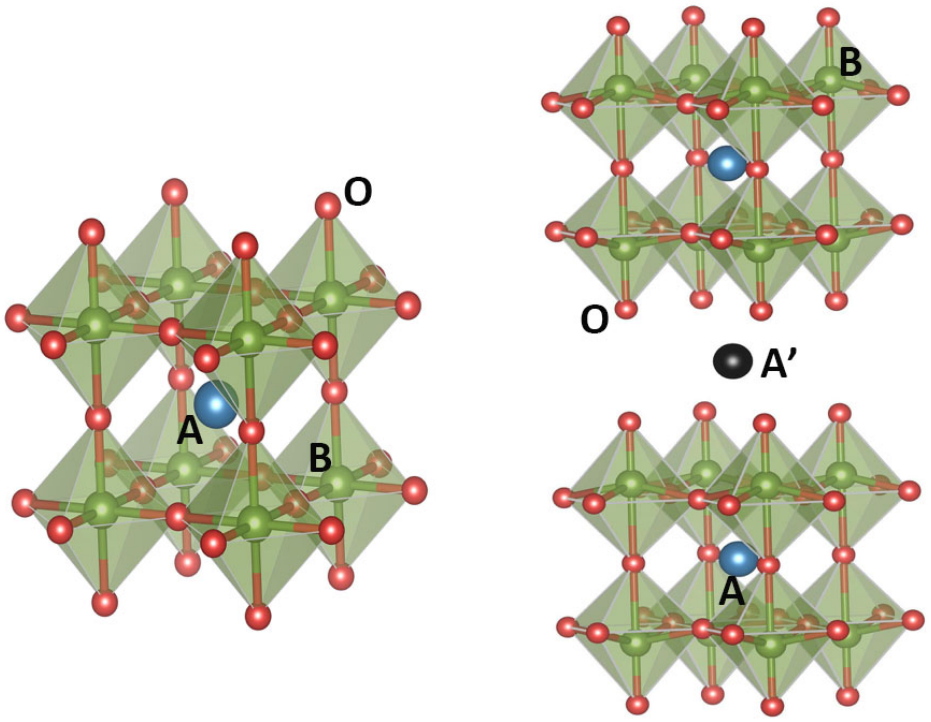

(a) (b)

Figure 1.1: (a) Structure of cubic perovskite with a chemical formula of ABO_3. (b) Structure of Dion-Jacobson phase with a chemical formula of $A_{(n-1)}A'B_nO_{(3n+1)}$ is presented here as an example of layered perovskite.

$$t = \frac{r_A + r_O}{\sqrt{2}\,(r_B + r_O)} \tag{1.1}$$

1.2 Perovskite in solid oxide fuel cell

The solid oxide fuel cell (SOFC) is one of the most promising clean energy-conversion technologies. Compared to traditional electric power generators, the SOFC exhibits many advantages. The SOFC can achieve high chemical-to-electrical conversion efficiency, without the emission of NO_x and CO_2.[13-14] Because of its high operating temperature, the SOFC is more flexible on hydrocarbon fuels, such as natural gas and diesel.[15] SOFC includes three main parts: anode, cathode and electrolyte. The dense electrolyte is sandwiched between electrodes. At anode, fuel is oxidized and electrons generated from fuel oxidation are transported to cathode through an external circuit. Anode must be porous to provide enough reaction sites and active for fuel oxidation. O_2 is absorbed and dissociates into O^{2-} at cathode. These oxide ions diffuse to the anode through a solid electrolyte. The electrodes in a SOFC are typically porous to obtain more reaction sites for fuel and oxygen. SOFC cells are usually connected to form a SOFC stack in industry.

Currently, application of SOFC is limited by several problems, such as high fabrication cost and high operating temperature. The high operating temperature (700 ~ 1000 °C) facilitates solid diffusion of oxide ion through the electrolyte. However, the high operating temperature causes several problems at the same time, such as material's thermal instability,[16-17] catalyst poisoning[18-19] and waste heat.[20] Current research on SOFCs focuses on reducing operating temperature while retaining adequate ionic conductivity. The lower operating temperature allows the selection of SOFC materials from a broader range and has less requirements on sealing materials and thermal management.[21] Perovskites have been widely used as anode, cathode and electrolyte. As anode materials with better thermal stability, several perovskites, such as La doped $SrTiO_3$,[22-23] have been developed to replace

the nickel/yttria-doped zirconia (YSZ) composite anode. Lanthanum strontium manganite based perovskites are the focus of cathode material research. Perovskites are investigated as electrolyte due to their high conductivity of oxide ion and proton. The following chapter of this dissertation focuses on the study of oxide ion diffusion mechanism in several Ruddlesden-Popper layered perovskite cathodes. A linkage is established between oxide ion transportation and specific perovskite octahedral rotation, which can contribute to the design of fast ionic transport cathode materials and lower SOFC's operating temperature.

1.3 Ferroelectricity in perovskites

Ferroelectricity in perovskites has become a popular research field due to its potential application in magnetoelectric devices.[24] Perovskites with similar structure and unit cell volume can display distinct ferroelectric behaviors. Several perovskites, such as $ATiO_3$ family, have been studied experimentally and computationally. For example, ferroelectricity in $ATiO_3$ materials have been found correlated with tolerance factor. When tolerance factor is smaller than 1, system energy can be reduced by cooperative octahedral rotation. However, when tolerance factor is larger than 1, material can be stabilized by the displacement of B-site atom from octahedral center. Ferroelectricity is only observed when tolerance factor is larger than 1 in $ATiO_3$ family, such as $BaTiO_3$. With the help of large A-site atomic radius, $BaTiO_3$ will experience an octahedral deformation, which contributes to its ferroelectric property. As the size of A-site atom decreases, tolerance factor decreases and space available for the ferroelectric octahedral deformation also decreases. When tolerance factor is around or smaller than 1, such as $CaTiO_3$, the limited space hinders octahedral deformation and keeps materials in

a cubic structure. Structural difference between $BaTiO_3$ and $CaTiO_3$ is shown in Figure 1.2.

Ferroelectricity in perovskites is sensitive to atomic structure. Strain has been widely used in the enhancement of ferroelectricity in perovskites.[25] Strain can be generated and controlled in thin films during the deposition of one material onto another. For example, magnetic and ferroelectric properties of $KTaO_3/KNbO_3$ and $BaTiO_3/SrTiO_3$ multilayers have been investigated as a function of layer thickness.[26-27] In our project, we used epitaxial strain as a tool to enhance ferroelectricity in $CaMnTi_2O_6$.

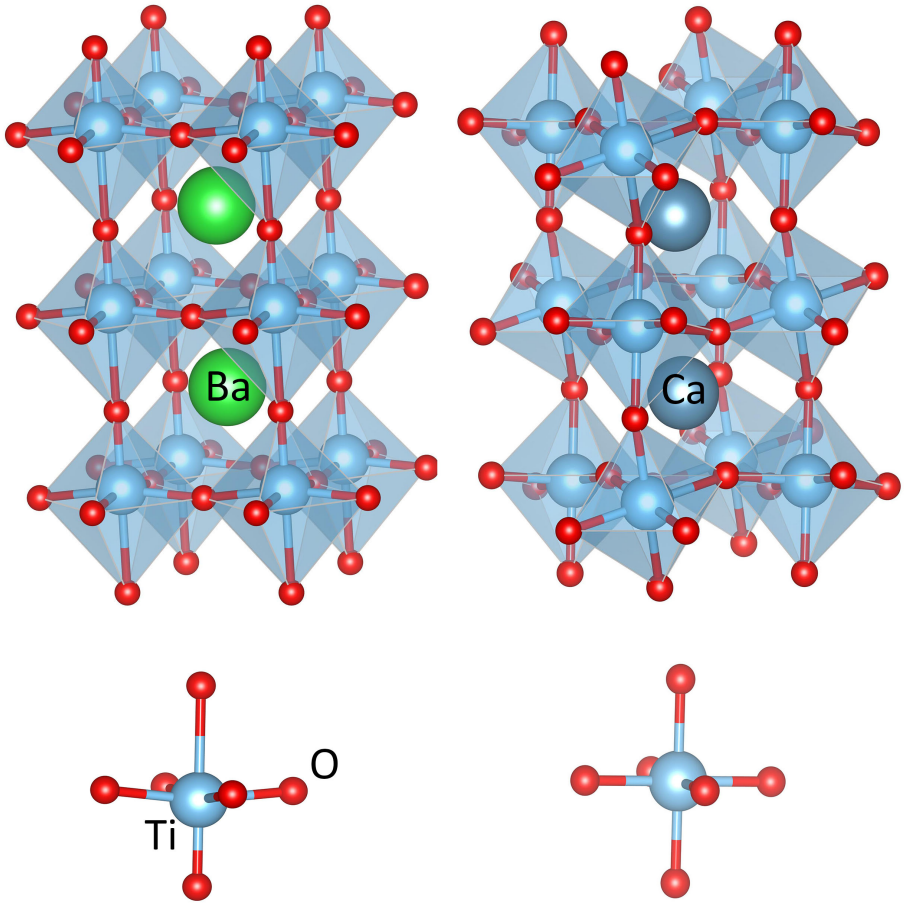

(a) (b)

Figure 1.2: (a) Structures of $BaTiO_3$ and deformed TiO_6 octahedron. The TiO_6 octahedral deformation produces an off-center displacement on Ti atoms and contributes to material's ferroelectricity. (b) Structures of $CaTiO_3$ and symmetrical TiO_6 octahedron. $CaTiO_3$ has smaller volume and not enough space for octahedral deformation. The tilted octahedral network reduces system energy and stabilized $CaTiO_3$.

1.4 Bulk modulus and octahedral rotation of $CaCu_3B_4O_{12}$ perovskite

Bulk modulus is used to measure the compressibility of a material. It describes how material's volume changes in response to an increase of external pressure. Bulk modulus can be calculated based on equation 1.2, where P is

pressure and V is volume. Bulk modulus is an important factor in the description of material's mechanical behavior and can significantly influence material's application.

$$K = -V\frac{dP}{dV} \tag{1.2}$$

Bulk modulus of perovskites has been widely investigated experimentally. Knowledge of a perovskite's hardness and stability is important especially where perovskite has application under high temperature or high pressure. In addition, due to perovskite's interesting insulator-metal transition,[28-29] ionic conduction[16] and ferroelectric properties,[30] thin-film perovskites have been widely used in semiconductor and green energy conversion industries. Mismatch between the thin-film and substrate lattice parameters will generate epitaxial strain during the synthesis and application of thin-film perovskites, which makes perovskite's mechanical behavior of great importance. Doping has been employed in perovskite fabrication to generate defects and destroy long-term ordering. Bulk modulus is an important mechanical behavior descriptor in the study of structural mismatch caused by doping.

$CaCu_3B_4O_{12}$ is a family of the A-site ordered perovskite oxides. People's attention has been attracted by their intriguing electric and magnetic properties. For example, $CaCu_3Ti_4O_{12}$ shows a large dielectric constant over a wide temperature range.[31-34] $CaCu_3Mn_4O_{12}$ is a ferromagnetic semiconductor with a Curie temperature range above room temperature.[35-36] A bulk modulus study on $CaCu_3B_4O_{12}$ family is used to provide us a better understanding of $CaCu_3B_4O_{12}$ perovskite's structural and physical property, especially knowledge on cooperative octahedral rotations.

Cooperative octahedral rotations, also called octahedral-site tilting, is one of the most important research focuses in perovskite studies. Octahedral distortions can be separated into two types: displacement of B-site atom and site-symmetry change. Group theory has been applied to the classification of octahedral tilting systems by considering specific titling pattern and corresponding subgroups.[37] Octahedral rotation has significant influence on perovskite's properties, such as phase transition. Bulk modulus can be associated with octahedral rotation because change in octahedral rotation can be induced by external pressure. My study in the third project investigated how octahedral rotations change under pressure and how octahedral rotation affect the bulk modulus.

Chapter 2

Enhancement of Ionic Transport in Complex Oxides through Soft Lattice Modes and Epitaxial Strain*

2.1 Abstract

Perovskites have received extensive research as electrodes in SOFC due to their high ionic conductivity. Octahedral tilting has been suggested as the origin of fast ionic transport through perovskites. In this work, we studied oxide ion diffusion through a series of $Ln_2NiO_{4+\delta}$ Ruddlesden-Popper phases ($Ln = La, Pr, Nd, Sm, Eu, Gd$) with first-principle density functional theory calculations. Both interstitial and interstitialcy[38] diffusion mechanisms of oxygen interstitial and oxygen vacancies have been simulated and interstitialcy mechanism is selected as the ionic transport mechanism due to their lower diffusion barriers. Soft lattice modes associated with interstitialcy mechanism are analyzed and a linkage is established between the 'softness' of specific structural distortions (so-called 'rotations' of the BO_6 octahedra) and oxygen migration energy barrier. We discovered that the magnitude of oxygen diffusion barrier is strongly correlated with the tendency of related octahedral rotation. We then proved that epitaxial tensile strain will reduce oxide ion diffusion barrier in Ruddlesden-Popper phases because epitaxial tensile strain can facilitate associated octahedral rotations. In addition, we discovered that the diffusion path becomes increasingly curved as the size of A-site cation decreases and explained how this curved diffusion path contributes to the reduction of ionic transport barrier. Our study provides some advices on the design of cathode materials for a lower operating temperature SOFC.

* This chapter is based on work published at Chem. Mater. 2015, 27, 2647-2652

2.2 Introduction

Extensive SOFC research focuses on techniques to reduce the operating temperature to 500 ~ 700 °C. The lower operating temperature has many advantages, such as less waste heat. However, the oxygen reduction reaction (ORR) introduces new challenges at lower operating temperature because the ORR kinetics is usually slow due to its high activation energy.[39] In addition, lower operating temperature will slow down ionic transport processes. Therefore, promising SOFCs cathode materials should possess both the properties of high catalytic activity and fast ionic transport ability. A common approach to overcome this problem is to replace traditional cathode materials with mixed ionic-electronic-conductors (MIEC).[40-41] Unlike traditional cathode materials where ORR can only occur at the air/electrode/electrolyte triple phase boundary, MIEC provides much larger reaction area and retains adequate ORR kinetics at much lower temperature by allowing ORR to happen on the whole electrode surface[42]. According to Adler,[43] the electrochemical behavior of MIEC highly depends on solid-state oxygen diffusion and O_2 surface exchange. We focused on understanding the solid-state oxygen diffusion process in this work.

Perovskite, such as $La_{1-x}Sr_xMnO_{3-\delta}$ (LSM), $La_{1-x}Sr_xCoO_{3-\delta}$ (LSC) and $La_{1-x}Sr_xFeO_{3-\delta}$ (LSF), have been extensively studied as promising MIEC materials.[44] Even though these materials exhibit good ionic transport properties, the low chemical[45] and thermal[46-47] stabilities at high operating temperature limit their applications. Recently, Ruddlesden-Popper layered phases attract peoples' interest as MIEC cathode materials.[48-49] Several Ruddlesden-Popper phases have been synthesized and investigated, such as La_2NiO_4 and Pr_2NiO_4. They exhibit a wide range of oxygen stoichiometry and good ionic transport property. However, the

mechanism and atomic source of this low temperature ionic transport is still unclear. Structural comparison between two end members ($n = 1$) of perovskite phase and layered Ruddlesden-Popper phase is shown in Figure 2.1. There are three migration mechanisms in perovskite: interstitial, interstitialcy and vacancy mechanism. Vacancy mechanism has been discovered in the ionic transport of simple perovskite materials.[50-52] Several research through first-principle and molecular dynamics calculations indicates interstitialcy as promising diffusion mechanism.[53-54]

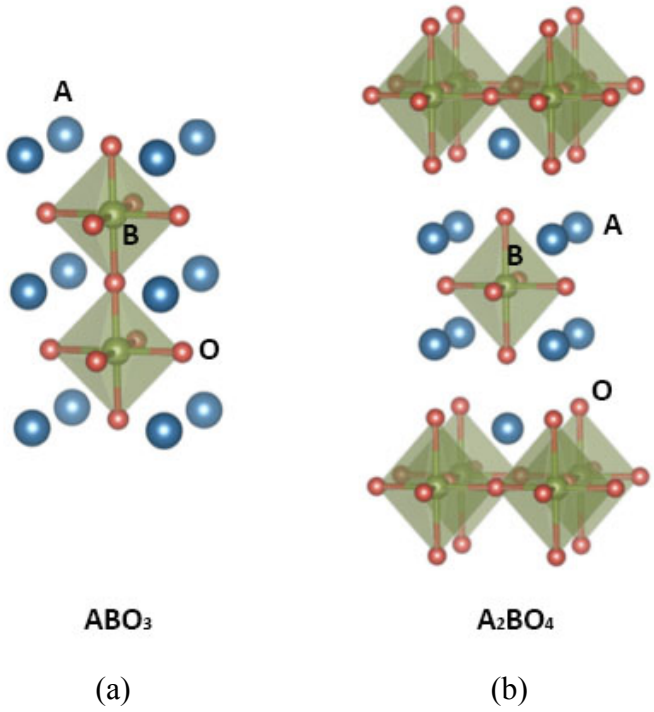

Figure 2.1: (a) Structure of perovskite with a chemical formula of ABO_3. (b) Structure of layered Ruddlesden-Popper phase with a chemical formula of $A_{n+1}B_nO_{3n+1}$ ($n = 1$).

It is widely believed that the tilting of octahedra has significant contribution to the ionic transport at low temperature and can be used in the design of new

SOFC materials. The objective of this work is to find the relationship between octahedral tilting and ionic transport property of Ruddlesden-Popper (RP) oxides, with the help of density functional theory calculation and symmetry mode of octahedral tilting. This relationship can serve as a principle in the design of new complex oxide materials for SOFCs. Octahedral-site titling in RP phases is analyzed through a symmetry mode approach. In this approach, octahedral-site tilting is linked to its parent structure in higher symmetry through some specific modes. As for the Ln_2NiO_4 materials, their parent phase is high temperature tetragonal (HTT) phase with space group $I4/mmm$.[46] The octahedral tilting is associated with parent phase through a X_3^+ irreducible mode. Nickelate RP phases go through a series of octahedral tilting transitions as temperature decreases. Their space group will change from $I4/mmm$ to Cmca and $P4_2/ncm$, as illustrated in Figure 2.2. The symmetry mode approach has been proved a powerful tool in octahedral tilting description and how easily each type of tilting will happen can be predicted based on phonon calculation of each symmetry mode.[55-57]

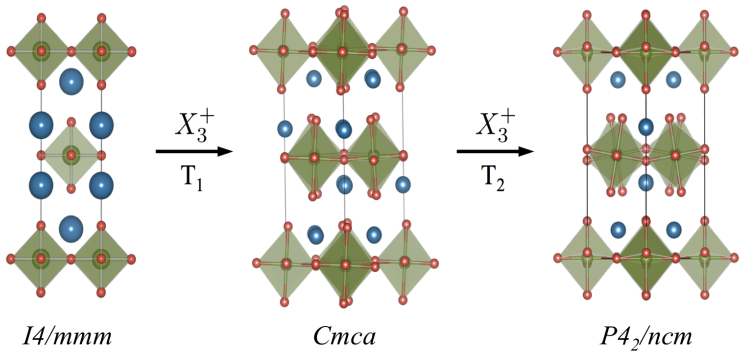

Figure 2.2: Phase transitions of nickelate RP phases with decreasing temperature (T_1>T_2). The octahedral tilting in these phase transitions follows the X_3^+ symmetry mode of HTT phase.

2.3 Computational method

First-principle density functional theory calculations were performed on six nickelate RP phase materials ($Ln_2NiO_{4+\delta}$ with $Ln = La, Pr, Nd, Sm, Eu, Gd$) using Vienna Ab Initio Simulation Package (VASP) with PBEsol+U functional.[58-59] We used the projector augmented wave (PAW) method and selected U = 4.5 eV as on-site Coulomb parameter and J = 0.7 eV as exchange parameter for Ni atom.[60] A series of U values were tested in our calculation and migration barrier showed no obvious dependence on the value of U, as shown in Table 2.1. Structures were simulated with 600 eV plane-wave cutoff and $6\times6\times4$ Monkhorst-Pack grid. Migration barriers were calculated using climbing image nudged elastic bands (CI-NEB) technique with a reduced $4\times4\times2$ Monkhorst-Pack grid.[61] Most CI-NEB calculations are based on RP phases with excess oxygen of 0.125. We also calculated the migration barrier with excess oxygen of 0.0625 and found that lower interstitial oxygen concentration will result in lower migration barrier. Migration barriers under different excess oxygen concentrations are shown in Table 2.2. There is no long range magnetic ordering at the high operating temperature of SOFC. Similar to Morgan's work,[62] ferromagnetic ordering was applied to all calculations. Oxygen migration barrier was simulated under different magnetic ordering and we found that the magnetic ordering has no significant influence on ionic migration process. All RP phases were simulated in the undistorted $I4/mmm$ space group. Lattice constants and tolerance factors of Ln_2NiO_4 are listed in Table 2.3.

Table 2.1: Dependence of migration barrier on U energy

Materials	Migration barrier / eV			
	U = 4.5 eV	U = 5.0 eV	U = 6.0 eV	U = 7.0 eV
$La_2NiO_{4.125}$	1.064	1.063	1.062	1.059
$Pr_2NiO_{4.125}$	0.915	0.914	0.913	0.912
$Nd_2NiO_{4.125}$	0.873	0.872	0.870	0.868

Table 2.2: Dependence of migration barrier on excess oxygen concentration

Materials	Migration barrier / eV	
	δ =0.125	δ =0.0625
La_2NiO_4	1.064	0.656
Pr_2NiO_4	0.915	0.535
Nd_2NiO_4	0.873	0.487
Sm_2NiO_4	0.814	0.424
Eu_2NiO_4	0.797	0.417
Gd_2NiO_4	0.762	0.379

Table 2.3: Lattice constant of the nickelate RP phases at the space group I4/mmm

Materials	a / Å	c / Å	tolerance factor
La_2NiO_4	5.4739	12.6357	0.977
Pr_2NiO_4	5.4046	12.3108	0.964
Nd_2NiO_4	5.3825	12.1941	0.957
Sm_2NiO_4	5.3462	11.9854	0.947
Eu_2NiO_4	5.3251	11.8936	0.942
Gd_2NiO_4	5.3179	11.8025	0.938

2.4 Results and discussion

2.4.1 Interstitial and interstitialcy migrations

Both interstitial and interstitialcy migration mechanisms were studied and compared through CI-NEB calculations. Interstitial migration mechanism is the interstitial oxygen directly hops into a nearby empty interstitial site inside x-y plane (site A to site D in Figure 2.3). While, interstitialcy migration mechanism is that the interstitial oxygen replaces a nearby apical oxygen of NiO_6 octahedron and kicks the apical oxygen to an empty interstitial site (site A to site B and site B to site C in Figure 2.3).[38] Our calculation showed that, for $Ln_2NiO_{4.125}$, interstitialcy migration mechanism has lower migration barrier than interstitial migration mechanism, as shown in Table 2.4. Our simulation agrees with Grimes' research using molecular dynamics calculation.[63] As a result, interstitialcy mechanism was selected as the ionic transport mechanism in the work. Figure 2.4 shows how interstitial oxygen atom is transported through interstitialcy mechanism.

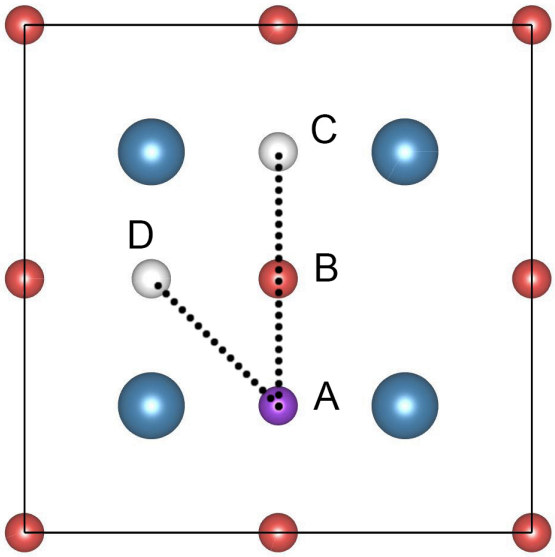

Figure 2.3: Comparison between interstitial and interstitialcy migration mechanisms from a view along z axis. Site A is the current interstitial atom, site B is a nearby apical oxygen atom of NiO_6 octahedron, site C and site D are empty interstitial sites.

Table 2.4: Migration barriers of interstitial and interstitialcy mechanisms for Ln2$NiO_{4.125}$ perovskites

Materials	Migration barrier / eV		
	$La_2NiO_{4.125}$	$Pr_2NiO_{4.125}$	$Nd_2NiO_{4.125}$
Interstitial mechanism barrier	1.9819	2.0410	2.0662
Interstitialcy mechanism barrier	1.0644	0.9151	0.8726

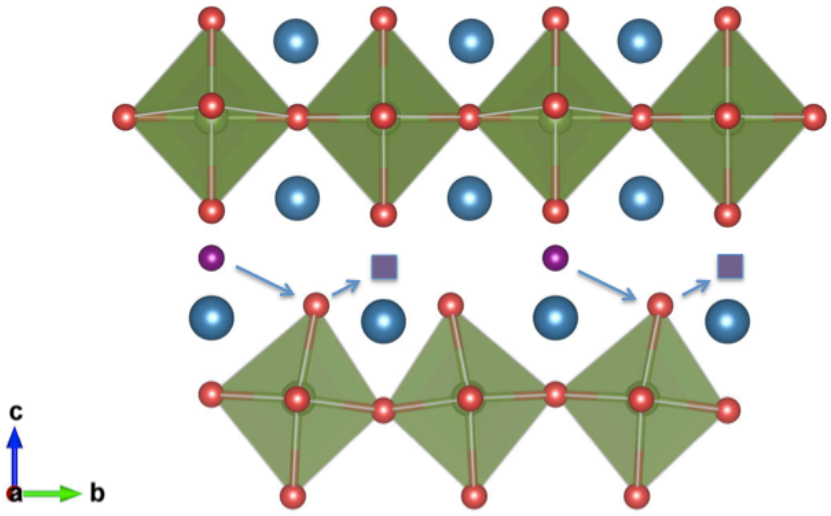

Figure 2.4: Snapshot of interstitialcy migration mechanism. An interstitial oxygen atom (purple) replaces a nearby apical oxygen atom. The replaced apical oxygen atom forms a new interstitial atom.

2.4.2 Octahedral tilting and interstitialcy migration barrier

The hypothesis of this study is that octahedral tilting has significant contribution to interstitialcy migration process and materials with softer octahedral tilting modes will have lower migration barrier. We found that the interstiticalcy migration process can be largely represented by the X_3^+ octahedral tilting mode under $I4/mmm$ space group. Force constant of X_3^+ octahedral tilting mode was used to describe the softness of octahedral tilting. All force constants were calculated through frozen phonon method.[64] As the size of A-site atom decreases, the force constant of X_3^+ octahedral tilting mode becomes more negative. In addition, epitaxial strain has been proved a useful tool in the control of octahedral rotation. We studied both X_3^+ force constant and migration barrier under epitaxial

tensile and compressive strains. Tensile and compressive strains were simulated by increasing and decreasing epitaxial lattice constant by 1.5%. As illustrated in Table 2.5, tensile strain will produce a softer X_3^+ octahedral tilting mode, while compressive strain will result in a harder X_3^+ octahedral tilting mode. Figure 2.5 shows the relationship between X_3^+ force constant and migration energy barrier. As the size of A-site atom decreases, the force constant of X_3^+ octahedral tilting mode becomes more negative and migration energy barrier decreases. Typically, reducing the size of A-site atom will result in a smaller unit cell volume and reduce space available for oxygen migration. However, in our study, material with smallest unit cell volume (Gd_2NiO_4) has the most negative X_3^+ octahedral tilting force constant and the lowest migration energy barrier. This proves our hypothesis that octahedral tilting plays a significant role in oxygen transport.

Table 2.5: Dependence of force constants on A-site atom and epitaxial strain

	Force constant of X_3^+ octahedral tilting mode / eV/Å^2		
Materials	compressive	equilibrium	tensile
La_2NiO_4	0.31	-0.32	-0.83
Pr_2NiO_4	-0.42	-1.08	-1.56
Nd_2NiO_4	-0.76	-1.44	-1.90
Sm_2NiO_4	-1.46	-2.09	-2.56
Eu_2NiO_4	-1.74	-2.43	-2.89
Gd_2NiO_4	-2.17	-2.77	-3.16

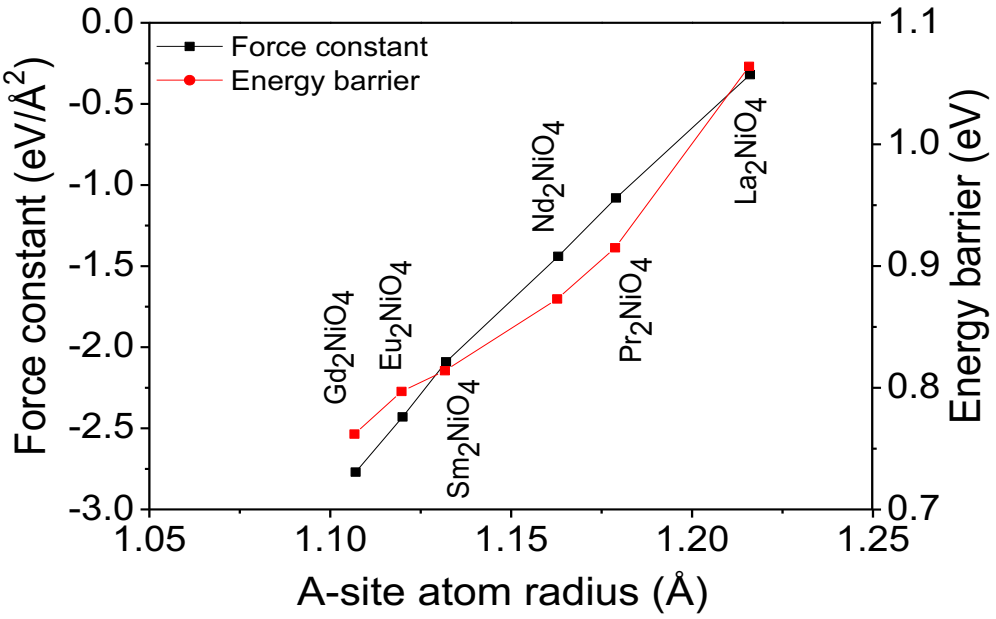

Figure 2.5: Influence of A-site atom radius on X_3^+ octahedral tilting force constant and migration energy barrier.

2.4.3 Influence of epitaxial strain on oxygen migration barrier

Octahedral tilting in perovskites is sensitive to external pressure,[65-67] which can be employed as a powerful tool in the control of X_3^+ octahedral tilting force constant. According to Table 2.5, tensile epitaxial strain produces a softer X_3^+ octahedral tilting mode and a lower oxygen migration energy barrier based on our hypothesis. From X_3^+ octahedral tilting illustrated in Figure 2.2, X_3^+ octahedral tilting will extend perovskite in x-y plane and shorten material along z-axis. The tensile epitaxial strain will provide more space inside x-y plane and facilitate X_3^+ octahedral tilting. CI-NEB calculations were performed under tensile and compressive epitaxial strains. Force constants of X_3^+ octahedral tilting mode and interstitialcy oxygen migration energy barriers are plotted in Figure 2.6, we discovered a linear relationship between X_3^+ octahedral tilting force constant and

oxygen migration energy barrier. A 1.5% tensile epitaxial strain can reduce interstitialcy migration barrier by about 0.5 eV. The limit of epitaxial strain within perovskite thin films depends on material's physical properties and synthesis techniques. The linear relationship indicates that specific octahedral tilting is a determinant factor in ionic transport through interstitialcy mechanism. For all six materials simulated in this study, tensile epitaxial strain will produce a more negative X_3^+ octahedral tilting force constant and reduce oxygen diffusion energy barrier.

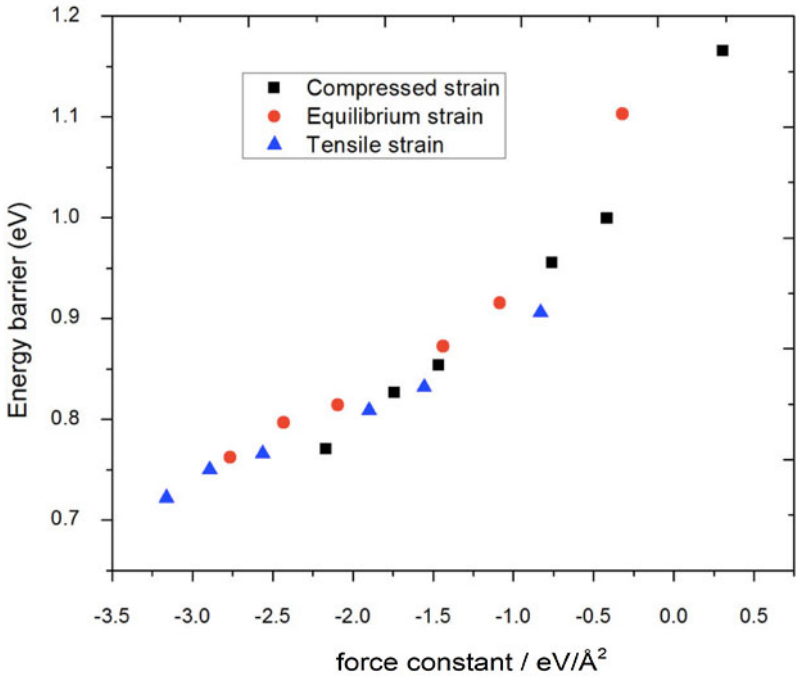

Figure 2.6: Relationship between X_3^+ octahedral tilting force constant and oxygen migration energy barrier of $Ln_2NiO_{4.125}$ materials. Tensile strain will decrease migration barrier, while compressive strain will produce a larger migration barrier.

2.4.4 Curved migration path

Due to the existence of interstitial oxygen atom and radius mismatch between A-site and B-site atoms, octahedra around interstitial oxygen atom tilts in the plane normal to the diffusion path. Even though this tilting normal to migration path is tiny compared with octahedral tilting along diffusion path, this small tilting will produce a curved migration path, which has a lower diffusion barrier than a straight migration path. I defined a tilting angle in Figure 2.7(a) and used it to measure the magnitude of octahedral tilting normal to the diffusion path. Tilting angles of materials with different A-site atoms and under different epitaxial strains are listed in Table 2.6. We found that smaller A-site atom and tensile epitaxial strain will result in a larger tilting angle normal to the migration path. Material with a more curved oxygen migration path will have a lower migration energy barrier. As A-site atom changes from La to Gd, the size of A-site atom and tolerance factor decreases, oxygen migration path becomes more curved, shown in Figure 2.7(b). La_2NiO_4 has smaller radius mismatch between A and B-site atoms than Gd_2NiO_4. So, the octahedral network in Gd_2NiO_4 is more tilted. In addition, Gd_2NiO_4 has smaller unit cell volume and space available for interstitial oxygen atoms is smaller. As a result, the interstitial oxygen atom will cause more octahedral tilting in Gd_2NiO_4 than La_2NiO_4. The energy barrier along a straight path was simulated by adding symmetry constrain into CI-NEB calculations and we found much higher migration energy barrier.

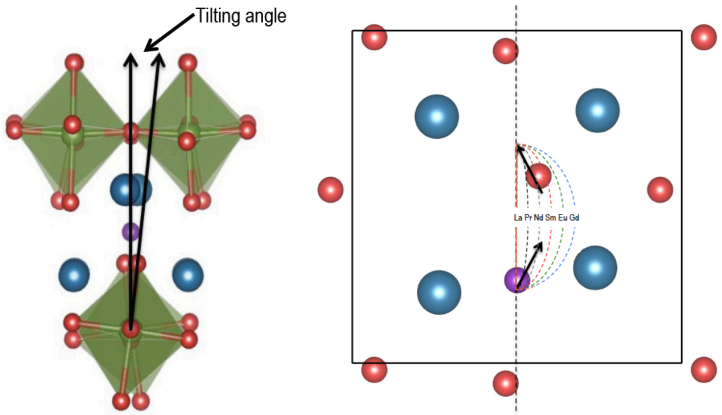

(a) (b)

Figure 2.7: (a) Octahedral tilting from a view along migration path. A tilting angle is defined to measure the amplitude of octahedral tilting normal to oxygen migration path. (b) Curved migration path of Ln_2NiO_4 with different A-site atoms from a view along z axis. As the size of A-site atom decreases, the migration path becomes more curved.

Table 2.6: Dependence of tilting angles on A-site atoms and epitaxial strain

Materials	Tilting angles normal to migration plane / ^{o}		
	compressed	equilibrium	tensile
$La_2NiO_{4.125}$	0.04	0.46	3.62
$Pr_2NiO_{4.125}$	0.37	4.75	5.73
$Nd_2NiO_{4.125}$	4.43	5.46	6.67
$Sm_2NiO_{4.125}$	5.78	6.81	7.37
$Eu_2NiO_{4.125}$	6.52	7.24	7.66
$Gd_2NiO_{4.125}$	6.81	7.49	7.67

Even though a curved migration path has been reported in several perovskites,[68-70] the role of a curved migration path is still unclear. By analyzing structural change along migration path using CI-NEB calculations, we discovered that the interstitialcy mechanism can be separated into two parts: the interstitial

oxygen atom goes through a triangle formed by A-site atoms and apical oxygen atom passes through another A-site atom triangle, as shown in Figure 2.8. As A-site atoms change from La to Gd, tolerance factor decreases and the octahedral network becomes more tilted. This octahedral tilting makes A-site atom triangles divert from isosceles triangle. In addition, Gd_2NiO_4 has a volume smaller than that of La_2NiO_4. Space available for oxygen interstitial in Gd_2NiO_4 is smaller than that in La_2NiO_4, indicating that interstitial will cause more deformation in Gd_2NiO_4. This deformation, together with octahedral network tilting, makes the A-site atom triangle in Gd_2NiO_4 diverts more from isosceles triangle. This makes Gd_2NiO_4's A-site atom triangles have larger area, resulting in larger space for oxygen to pass through. As a result, Gd_2NiO_4 has the smallest ionic transport energy barrier and unit cell volume at the same time among the Ln_2NiO_4 perovskites we studied in this project. Shape change of A-site atom triangles with the change of A-site atoms is shown in Figure 2.9 and the A-site atom triangle areas of Ln_2NiO_4 materials are listed in Table 2.7.

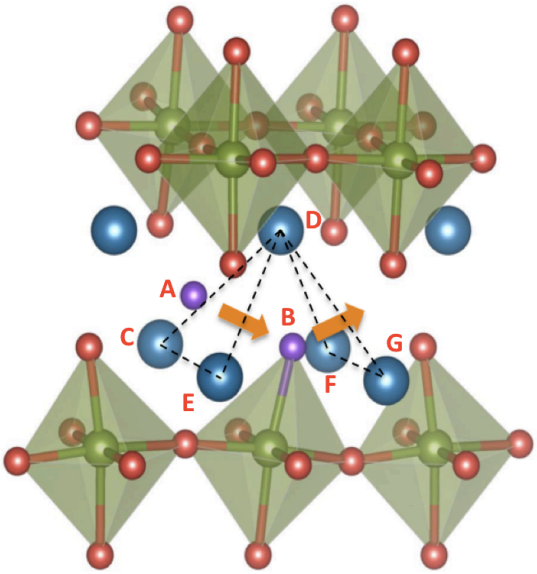

Figure 2.8: Graphic illustration of interstitialcy mechanism. Interstitial oxygen atom (A) will go through A-site atom triangle (CDE) and apical atom (B) will cross another A-site triangle (DFG) during interstitialcy migration.

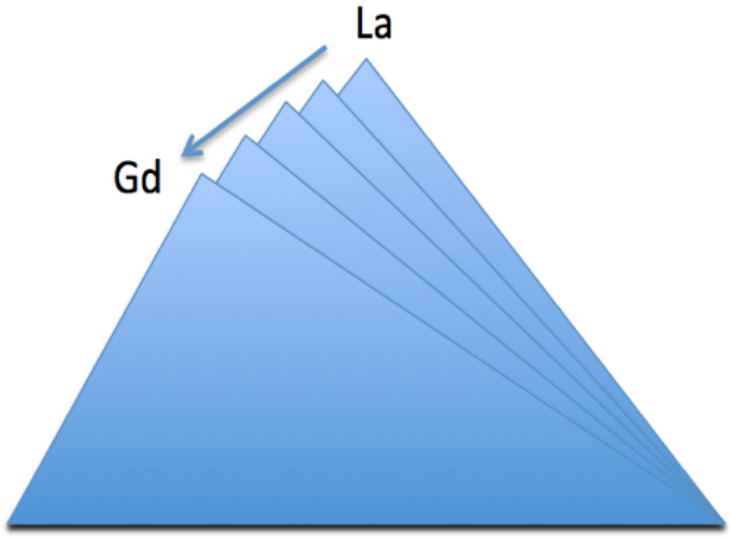

Figure 2.9: Shape change of A-site atom triangles as A-site atom changes from La to Gd.

Table 2.7: Area of A-site atom triangles

Materials	Area of A-site atom triangle / Å^2
$La_2NiO_{4.125}$	1.3197
$Pr_2NiO_{4.125}$	1.3357
$Nd_2NiO_{4.125}$	1.3446
$Sm_2NiO_{4.125}$	1.3610
$Eu_2NiO_{4.125}$	1.3644
$Gd_2NiO_{4.125}$	1.3583

2.4.5 Formation energy of oxygen interstitial

Interstitial formation energy played another import role in the oxygen transport of a SOFC. High interstitial formation energy will limit the amount of excess oxygen and hinder the ionic transport process. Both the size of A-site atom and epitaxial strain will affect the oxygen interstitial formation energy, based on an oxygen chemical potential equals to 5.1 eV.[71] Formation energy of oxygen interstitials is listed in Table 2.8. We found that, in contrast to migration energy barrier, smaller A-site atom and epitaxial tensile strain will increase oxygen interstitial formation energy. A smaller A-site atom will lead to a smaller volume. Space available for the formation of oxygen interstitial in material with smaller volume is quite limited. As a result, interstitial oxygen will cause larger strain and deformation in material with smaller A-site atom, generating a larger interstitial formation energy. As the performance of SOFCs is influenced by both defect formation and ionic transport, design of perovskite as new MIEC materials need to consider the balance between these two processes.

Table 2.8: Formation energy of interstitial oxygen in $Ln_2NiO_{4.125}$ perovskites

Material	Formation energy of interstitial oxygen / eV
$La_2NiO_{4.125}$	1.168
$Pr_2NiO_{4.125}$	2.012
$Nd_2NiO_{4.125}$	2.529
$Sm_2NiO_{4.125}$	3.769
$Eu_2NiO_{4.125}$	5.022
$Gd_2NiO_{4.125}$	5.021

2.4.6 Comparison with experiments

As the radius mismatch between A and B-site atom increases (from La to Gd), tolerance factor decreases and material synthesis becomes more difficult. Currently, ionic transport has been reported in $La_2NiO_{4+\delta}$, $Pr_2NiO_{4+\delta}$ and $Nd_2NiO_{4+\delta}$. The measured oxygen migration barrier of $La_2NiO_{4+\delta}$ varies from 0.2 to 0.9 eV, depends on the format of samples.[53-54, 72] Single crystal $Pr_2NiO_{4+\delta}$ and $Nd_2NiO_{4+\delta}$ have been reported with energy barriers of 0.7 and 1.4 eV.[73] Compared to experimental results, our simulation overestimated migration barrier of $La_2NiO_{4+\delta}$ and $Pr_2NiO_{4+\delta}$, while underestimated that of $Nd_2NiO_{4+\delta}$. It is well known that diffusion energy barriers are sensitive to temperature, concentration of oxygen interstitials and strain. Our overestimation on $La_2NiO_{4+\delta}$ and $Pr_2NiO_{4+\delta}$ migration barrier may come from the difference of oxygen interstitial concentration between simulation and experiments. To prove this, we simulated the migration energy barrier when δ equals to 0.0625 and found that migration barrier decreases

with the reduction of oxygen interstitial. Interstitial migration barriers of lower interstitial concentration systems are listed in Table 2.9.

Table 2.9: Simulated interstitial migration barrier of $Ln_2NiO_{4.0625}$ and $Ln_2NiO_{4.125}$

Material	Migration barrier / eV	
	$\delta = 0.0625$	$\delta = 0.125$
$La_2NiO_{4+\delta}$	0.656	1.064
$Pr_2NiO_{4+\delta}$	0.535	0.915
$Nd_2NiO_{4+\delta}$	0.487	0.873
$Sm_2NiO_{4+\delta}$	0.424	0.814
$Eu_2NiO_{4+\delta}$	0.417	0.797
$Gd_2NiO_{4+\delta}$	0.379	0.762

Experiment on $Nd_2NiO_{4+\delta}$ provides contradicting observation with our simulation. Oxygen interstitial diffusion are slower in $Nd_2NiO_{4+\delta}$ than those in $La_2NiO_{4+\delta}$ and $Pr_2NiO_{4+\delta}$ in experiments. There is no clear explanation for the difference between experiment and simulation on $Nd_2NiO_{4+\delta}$. One explanation is that $La_2NiO_{4+\delta}$'s smaller c lattice parameter dominates interstitial migration.[73] However, our study shows that the octahedral rotation plays a significant role in ionic transport and smaller unit cell volume can have lower migration energy barrier. One possible cause of the high migration barrier in $Nd_2NiO_{4+\delta}$ is that $Nd_2NiO_{4+\delta}$ has higher interstitial formation energy and interstitial formation energy becomes dominant factor in ionic transport when A-site atom changes from La to Nd.

The difficulty in material synthesis and diffusivity measurement limit the amount of experimental observations available. Current measurements are based on

different sample formats (thin film, bulk or single crystal), temperature and strain. These differences in experiments make it hard to obtain a consistent comparison on ionic transport ability of Ln_2NiO_4 perovskites. In addition, ionic transport ability is highly dependent on formation of oxygen interstitial and the relationship between interstitial diffusion and formation requires further study.

2.5 Conclusion

Our study shows significant role that octahedral rotation mode plays in ionic transport and how to enhance interstitial migration by softening related octahedral rotation mode. We have established a relationship between ionic transport and octahedral rotation mode in Ruddlesden-Popper materials through first-principle calculations. We proved that ionic transport in $Ln_2NiO_{4+\delta}$ materials follows interstitialcy diffusion mechanism and is highly dependent on specific octahedral rotation mode. Through CI-NEB calculations, we discovered that interstitialcy mechanism is associated with X_3^+ octahedral rotation mode and ionic migration barrier can be predicted based on the softness of X_3^+ mode. Force constant is used to describe the softness of symmetry mode and we obtained a linear relationship between the force constant of X_3^+ mode and migration energy barrier. Many factors can influence octahedral rotation in perovskites. We simulated epitaxial strain's influence on X_3^+ octahedral rotation and interstitial diffusion. We found that epitaxial tensile strain can soften X_3^+ octahedral rotation and reduce migration barrier. A curved diffusion path, resulting from octahedral tilting and interstitial atom, has been discovered in $Ln_2NiO_{4+\delta}$ perovskites. Even though cell volume decreases as A-site atom changes from La to Gd, a more tilted structure creates larger space for ionic migration and decreases migration energy

barrier. Ionic transport in $Ln_2NiO_{4+\delta}$ depends on both ionic migration barrier and defect formation energy. Our simulation shows that interstitial formation energy increases as A-site atom change from La to Gd. The design of $Ln_2NiO_{4+\delta}$ perovskites as cathode material of SOFC requires consideration on the balance between interstitial migration and defect formation.

2.6 Acknowledgements

This work is supported by a Ralph E. Powe Junior Faculty Enhancement Award from Oak Ridge Associated Universities. All our calculations are performed on the facility of Texas Advanced Computing Center. We thank Penghao Xiao for his assistance on CI-NEB calculations. We also thank Dane Morgan for his helpful discussion.

Chapter 3

New Mechanism for Ferroelectricity in the Perovskite $CaMnTi_2O_6$*

3.1 Abstract

Ferroelectricity in perovskites has been attractive research topic for many years. The origin of ferroelectricity in $BaTiO_3$ and $PbTiO_3$ has been extensively investigated and a corresponding displacement mode has been discovered. A-site atom with lone pair electrons and a tolerance factor larger than one have been considered as requirement of the existence of ferroelectricity. In this project, we discovered that $CaMnTi_2O_6$ is the only material that violates previous experience. We discovered ferroelectricity in $CaMnTi_2O_6$ with a Curie temperature of 650 K. Different from other ferroelectric perovskites, ferroelectricity in $CaMnTi_2O_6$ is caused by an order-disorder transition, instead of a specific displacive mode. The new origin of ferroelectricity in perovskite can facilitate material design and production of microelectronic devices. Neutron powder diffraction has been conducted to investigate the interaction between magnetic ordering and ferroelectric displacement. Density functional theory calculations were employed to find the origin of ferroelectricity and an explanation of the atomic configuration of coplanar Mn atoms. Similar double perovskites with different B-site atoms have been simulated and we find that $CaMnGe_2O_6$ has stronger ferroelectricity. A 1.5% compressive strain is applied to the simulation of $CaMnTi_2O_6$ and results in about 16.5% enhancement of the dipole moment.

* This chapter is based on work published at J. Am. Chem. Soc. 2018, 140, 2214-2220

3.2 Introduction

Ferroelectric perovskites attract extensive attention due to their potential application in magnetoelectric devices. Even though perovskites have diversified structures and various combinations of A and B-site atoms, ferroelectric perovskites are quite limited.[74] Because octahedral rotation alone cannot produce a polar perovskite structure. It has been believed that octahedral rotation will relax the mismatch between A-O and B-O bond length.[75] Deformation of BO_6 octahedra, which usually produces a polar structure, is caused by the electronic preference of B-site atom. So, octahedral rotation and deformation have different driving forces. $ATiO_3$ family perovskites have been extensively researched as ferroelectric materials. Large tolerance factor and A-site atom with lone-pair electrons have been proved important requirements for ferroelectricity. When A-site atom has s^2 lone-pair electrons and tolerance factor is larger than one, a ferroelectric displacement appears, creating asymmetric B-O bonds and ferroelectricity. When tolerance factor is close or smaller than one, a cooperative octahedral rotation is energetically favorable and lowers structural symmetry, shown in Figure 1.2. As the size of A-site atom decreases, unit cell volume decreases and space available for ferroelectric displacement decreases. As a result, for perovskites with smaller tolerance factor, cooperative octahedral rotation is energetically preferred relative to ferroelectric displacement, producing a nonferroelectric perovskite.

Benedek has provided an explanation on the question 'Why are there so few perovskite ferroelectrics?' through first-principle calculations and symmetry mode approach.[74] The $a^-a^-c^+$ tilting system is separated into $a^-a^-c^0$ and $a^0a^0c^+$ subsystems and is analyzed under space group Pbnm, which is the most common space group of ABO_3 family perovskites. Simulation shows that the displacement

of the A-site cation suppresses ferroelectricity when tolerance factor is small. Double perovskites have more complicated octahedral tilting system and A-site atom ordering. Several density functional theory studies predict the existence of polar double perovskites.[76-77] However, none of them has been proved experimentally. We discovered that $CaMnTi_2O_6$ is the only switchable ferroelectric double perovskite that is Pb^{2+} or Bi^{3+} free.[78-79]

$CaMnTi_2O_6$ has a polar space group $P4_2mc$ and is the only compound discovered in this space group. The B-site Mn^{2+} has two types of sites: coplanar and tetrahedral sites. At high temperature, $CaFeTi_2O_6$ and $CaMnTi_2O_6$ have similar crystal structures (space group $P4_2/nmc$). Under space group $P4_2/nmc$, coplanar Mn^{2+} will stay above or below MnO_4 plane randomly. In contrast, even though the space group allows $Fe^{2+}$to be out of the FeO_4 plane, Fe^{2+} will only stay inside the FeO_4 plane. High temperature structural difference between $CaMnTi_2O_6$ and $CaFeTi_2O_6$ is in Figure 3.1. When temperature is lower than Curie temperature, the displacement of all coplanar Mn^{2+} will align the same direction along c-axis, shown in Figure 3.2. As $CaFeTi_2O_6$ is a nonpolar perovskite, the ferroelectricity in $CaMnTi_2O_6$ is believed caused by the displacement of coplanar Mn^{2+}. DFT calculations are used to explore the driving force of the displacement of coplanar Mn^{2+} and the origin of ferroelectricity.

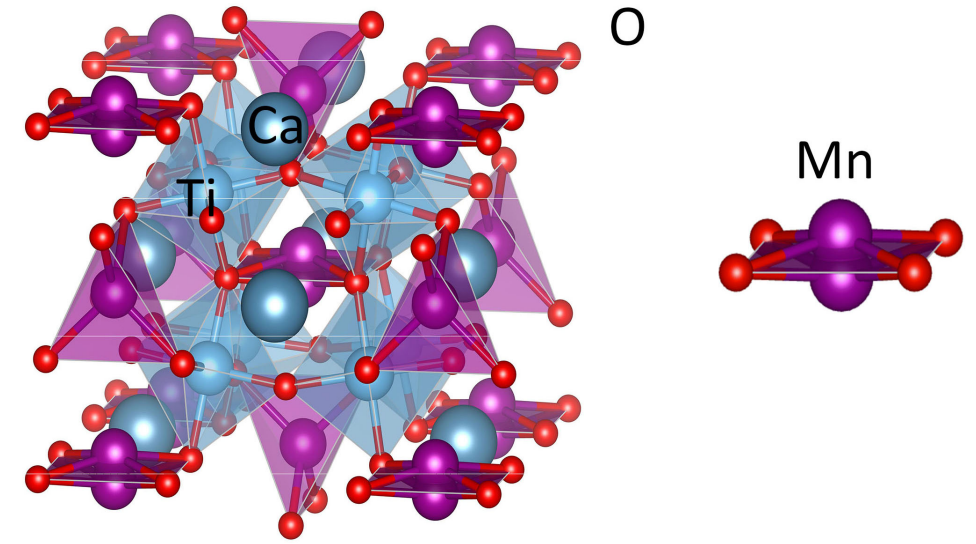

(a)

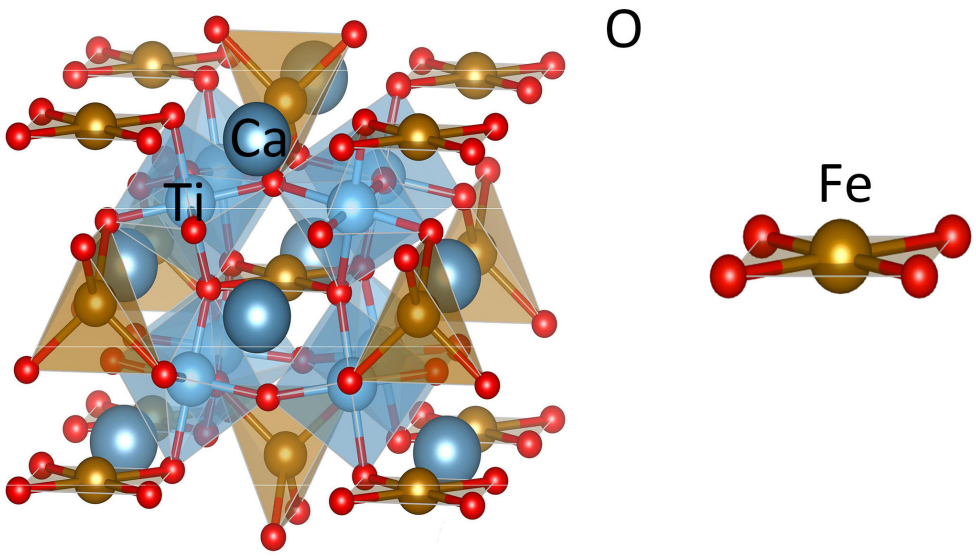

(b)

Figure 3.1: (a) Structure of nonpolar $CaMnTi_2O_6$ and displacement of Mn^{2+} in MnO_4 coplanar. At temperature above Curie temperature, the displacement of Mn^{2+} distributes randomly above or below MnO_4 coplanar. (b) Structure of $CaFeTi_2O_6$ and FeO_4 coplanar.

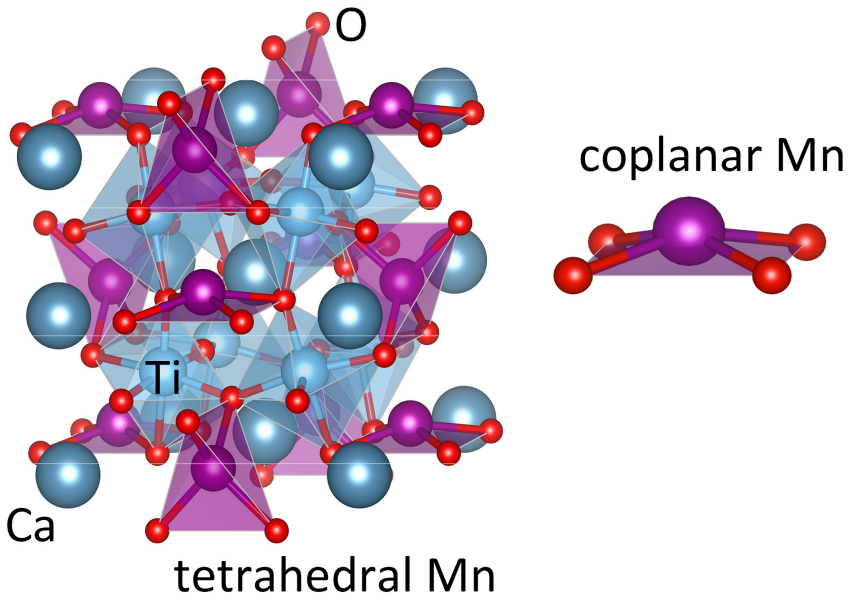

Figure 3.2: Structure of polar $CaMnTi_2O_6$ and displacement of Mn^{2+} in MnO_4 coplanar. In polar phase, coplanar Mn^{2+} are ordered along c axis.

3.3 Computational method

First-principle density functional theory calculations were performed on $CaMnTi_2O_6$ and $CaFeTi_2O_6$ with Vienna Ab Initio Simulation Package (VASP) and PBEsol+U functional.[58-59] Projected augmented wave (PAW) was selected in the simulation.[60] The selection of on-site Coulomb parameter U and exchange parameter J for Mn, Fe and Ti atoms are listed in Table 3.1. Several choices of U and J were tested and they showed no significant influence on simulation results. Structural calculations were performed with 600 eV plane-wave cutoff and 6×6×6 Monkhorst-Pack grid. A 15×15×15 Monkhorst-Pack grid was employed in the density of states calculation to achieve higher accuracy.

Table 3.1: Selection of U and J in PEBsol+U calculations

Atom	U / eV	J / eV
Mn	4.5	0.7
Fe	4.5	0.7
Ti	5.0	0.6

3.4 Results and discussion

3.4.1 Structure and magnetic ordering

Both polar $CaMnTi_2O_6$ and nonpolar $CaFeTi_2O_6$ phases have been simulated in our study. $CaFeTi_2O_6$ was relaxed under $P4_2mc$ and $P4_2/nmc$ space groups with symmetry constraint. We found that the artificial polar $CaFeTi_2O_6$ will change into nonpolar phase during structural relaxation, which agrees with our experimental observation. Because of the periodical boundary condition in density functional theory calculations, we cannot simulate the random displacement of coplanar Mn^{2+}. $CaMnTi_2O_6$ was simulated under low temperature polar ($P4_2mc$) and nonpolar ($P4_2/nmc$) phases. $CaMnTi_2O_6$ was relaxed into $P4_2mc$ space group in both simulations. Energy of several magnetic orderings have been calculated and compared through DFT calculations, shown in Table 3.2. Based on our simulation, $CaMnTi_2O_6$ has a ground state of polar phase and C-type antiferromagnetic ordering. The energy difference between C-type antiferromagnetic polar phase and G-type antiferromagnetic polar phase is very small, indicating a very weak magnetic interaction between tetrahedral and coplanar Mn^{2+} inside column. Our finding is compatible with a weak antiferromagnetic $Mn^{2+} - O - O - Mn^{2+}$

superexchange interaction between Mn^{2+}.[79] Structures and magnetic ordering of C-type and G-type antiferromagnetic polar phases of $CaMnTi_2O_6$ have been plotted in Figure 3.3. In addition, we discovered that the displacement of coplanar Mn^{2+} is 0.009 Å and C-type antiferromagnetic ordering can enhance the displacement of coplanar Mn^{2+}.

Weak exchange interactions have been discovered in both $CaMnTi_2O_6$ and $CaMnFe_2O_6$, which make comprehensive dipole-dipole interaction. Magnetic interactions in $CaMnTi_2O_6$ and $CaFeTi_2O_6$ were simulated and analyzed with DFT calculations. Energies of $CaFeTi_2O_6$ with different magnetic configurations are listed in Table 3.3. Ferromagnetic ordering has the lowest energy in our simulations. However, the energy difference between ferromagnetic and C-type antiferromagnetic ordering is very small. Clear observation and explanation on magnetic interactions within $CaFeTi_2O_6$ is still challenging from an experimental point of view.

Magnetic interactions of $CaMnTi_2O_6$ and $CaFeTi_2O_6$ were calculated by fitting energies of various magnetic configurations to the Ising model. The Ising model has been widely employed in the study of 2D and 3D magnetization.[80-81] In our Ising model calculation, perovskites are simplified into 3D magnetic network of Mn^{2+} and Fe^{2+}. Each site in the 3D magnetic network can only take either a positive or negative vector to represent dipole. The length of vector is used to represent the amplitude of dipole moment and its sign indicates the direction of the dipole. The simplified 3D magnetic network is shown in Figure 3.4. Four types of dipole interactions were included in our calculation: columnar interaction (tetrahedral-coplanar interaction along z-axis), in-plane interaction (tetrahedral-coplanar interaction within x-y plane), tetrahedral-tetrahedral interaction and

coplanar-coplanar interactions. Magnetic coupling energy of $CaMnTi_2O_6$ and$CaFeTi_2O_6$ are listed in Table 3.4 and 3.5. We discovered that the coupling energies of coplanar-coplanar interaction and tetrahedral-tetrahedral interaction are tiny compared to other interactions of $CaMnTi_2O_6$, which agrees with our observation that C-type and G-type antiferromagnetic $CaMnTi_2O_6$ are close in energy. This calculated result can be explained by the large coplanar-coplanar and tetrahedral-tetrahedral distance. For $CaFeTi_2O_6$, its magnetic interaction between tetrahedral sites is very small, which is similar to the case of $CaMnTi_2O_6$. However, the tetrahedral-coplanar interaction along z-axis in $CaFeTi_2O_6$ is much stronger than other interactions. As a result, compared to coplanar Mn^{2+}, relatively large magnetic dipole interaction exists between coplanar Fe^{2+}.

Kinetic Monte Carlo simulation was conducted to analyze how the dipole-dipole interactions affect the magnetic property in $CaMnTi_2O_6$ and $CaFeTi_2O_6$.[82] We found that , even though their structures are similar to each other, $CaMnTi_2O_6$ and $CaFeTi_2O_6$ show distinct magnetic behaviors. As shown in Figure 3.5, spins in $CaMnTi_2O_6$ become ordered at a temperature between 20-40 K. Defects in magnetic ordering is observed at 20 K. When temperature is lowered to 10 K, all magnetic ordering defects disappear. Figure 3.6 shows how the magnetic structure of $CaFeTi_2O_6$ changes with temperature. $CaFeTi_2O_6$ is paramagnetic at 40 K. When temperature is decreased to 10 K, short-range magnetic ordering along z-axis is formed. At 7 K, long range ferromagnetic ordering along z-axis exist and there are a lot of magnetic ordering defects. At 5 K, magnetic domains appear whereas most magnetic ordering defects disappear. Within a magnetic domain, $CaMnTi_2O_6$ is C-type antiferromagnetic ordering, while $CaFeTi_2O_6$ is ferromagnetic ordering. Magnetic ordering within domains in these two perovskites agrees with our DFT

ground-state calculations. For $CaFeTi_2O_6$, the long range magnetic ordering along z-axis is consistent with its large coupling energy along z-axis. An interesting difference between $CaMnTi_2O_6$ and $CaFeTi_2O_6$ is that the domain boundary of $CaMnTi_2O_6$ is normal to z-axis, while the domain boundary of $CaFeTi_2O_6$ is along z-axis. In addition, the magnetic ordering change with external field is simulated for $CaFeTi_2O_6$, as shown in Figure 3.7. In our simulation, a ferromagnetic sample of $CaFeTi_2O_6$ is used as starting configuration. Then, external field along reverse direction is applied to the sample. We discovered that the strong coupling interaction along z-axis leads to a columnar change of dipole direction. One dipole direction change induce nearby dipole direction change within the column. Our observation may provide a dynamical explanation on interesting phenomena observed in some 1D magnetic materials, such as $Ca_3Co_2O_6$.[83]

Table 3.2: The magnetic ordering and corresponding ground state energy of $CaMnTi_2O_6$

Magnetic ordering	Energy per unit formula / eV
Ferro-$P4_2mc$	0.0031
A-type-antiferro- $P4_2mc$	0.0036
C-type-antiferro-$P4_2/nmc$	0.0024
C-type-antiferro- $P4_2mc$	0.0
G-type-antiferro- $P4_2mc$	0.0006

Table 3.3: The magnetic ordering and corresponding ground state energy of $CaMnTi_2O_6$

Magnetic ordering	Energy per unit formula / eV
Ferro	0.0
A-type-antiferro	0.0037
C-type-antiferro	0.0005
G-type-antiferro	0.0066

Table 3.4: Coupling energy of dipole interactions in $CaMnTi_2O_6$

Type of dipole interaction	Coupling energy / eV
columnar interaction	-0.000523
in-plane interaction	0.000773
coplanar-coplanar interaction	0.000004
tetrahedral-tetrahedral interaction	-0.000004

Table 3.5: Coupling energy of dipole interactions in $CaFeTi_2O_6$

Type of dipole interaction	Coupling energy / eV
columnar interaction	-0.000611
in-plane interaction	-0.000106
coplanar-coplanar interaction	0.000079
tetrahedral-tetrahedral interaction	-0.000006

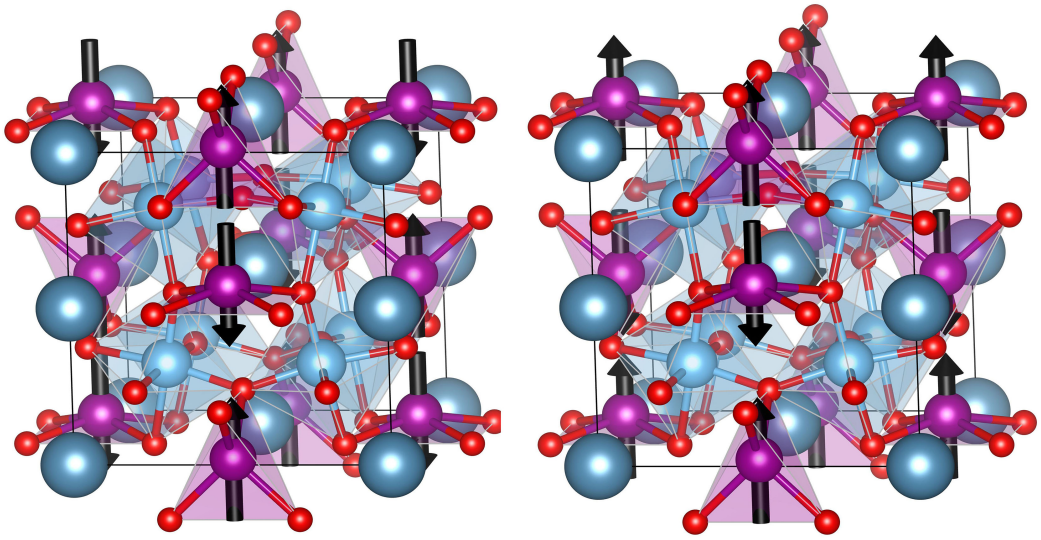

(a) (b)

Figure 3.3: Structures and magnetic ordering of C-type (a) and G-type (b) antiferromagnetic ordering of polar $CaMnTi_2O_6$ phases.

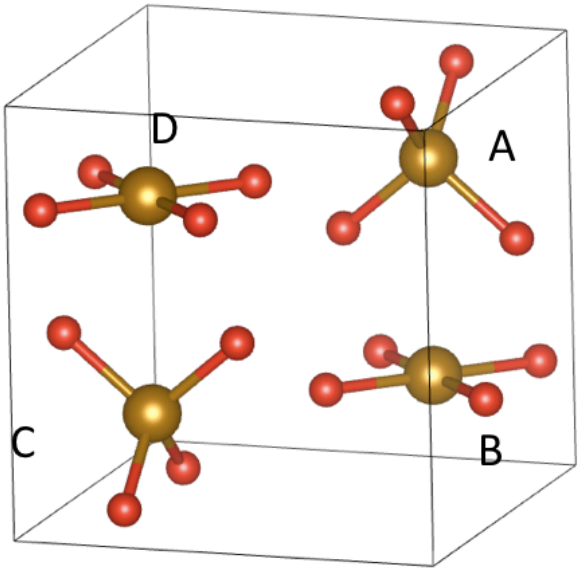

Figure 3.4: The simplified 3D Fe^{2+} network used in Ising model calculation. Four magnetic interactions are included: columnar interaction (A and B), in-plane interaction (B and C), coplanar-coplanar interaction (B and D) and tetrahedral-tetrahedral interaction (A and C).

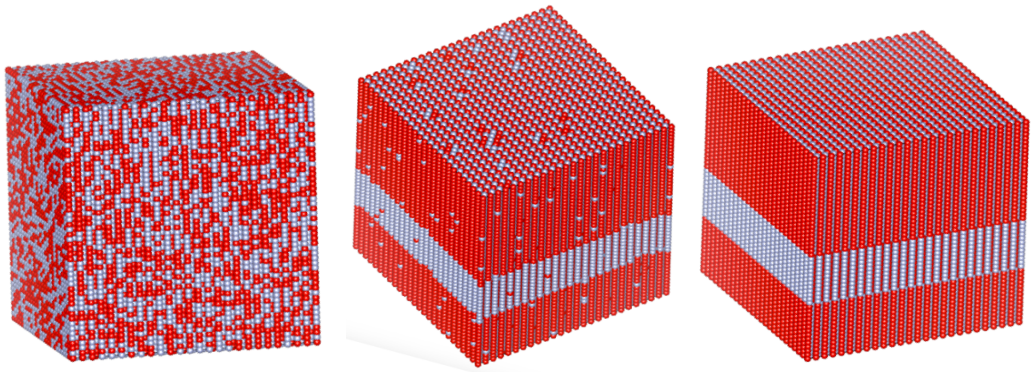

(a) (b) (c)

Figure 3.5: The spin structure of $CaMnTi_2O_6$ at 40 K (a), 20 K (b) and 10 K (c). Red and grey dots are used to represent dipole directions. Red dot indicates a dipole direction along positive z-axis, while white dot has a dipole direction along negative z-axis. Samples in (b) and (c) are rotated to show magnetic defects.

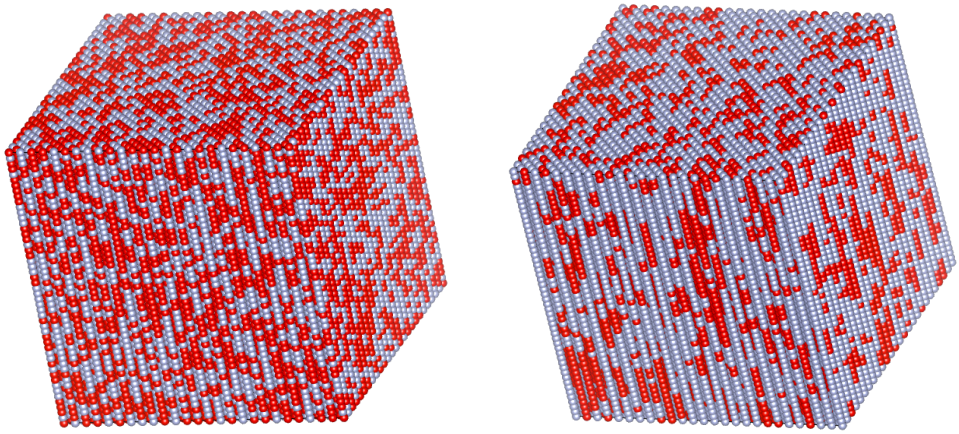

(a) (b)

Figure 3.6 (continued on next page, legend follows)

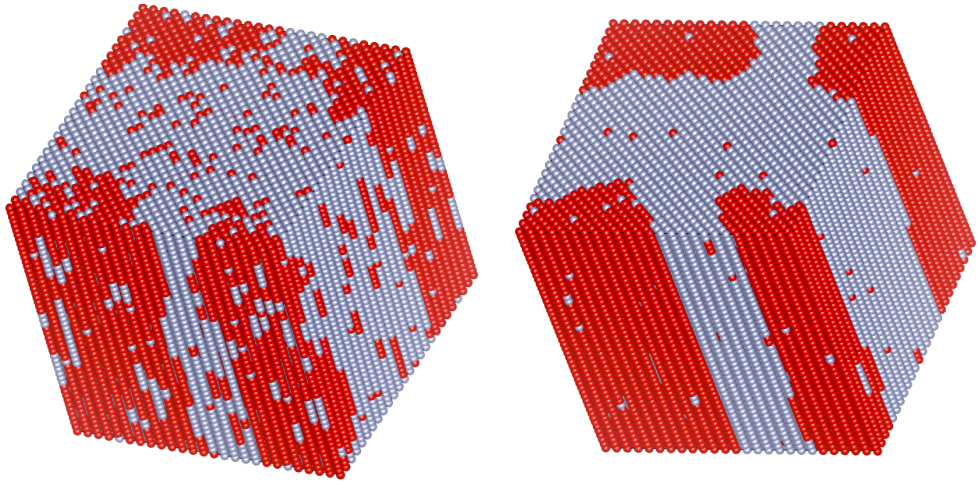

(c) (d)

Figure 3.6: The spin structure of $CaMnFe_2O_6$ at 40 K (a), 10 K (b), 7 K (c) and 5 K (d).

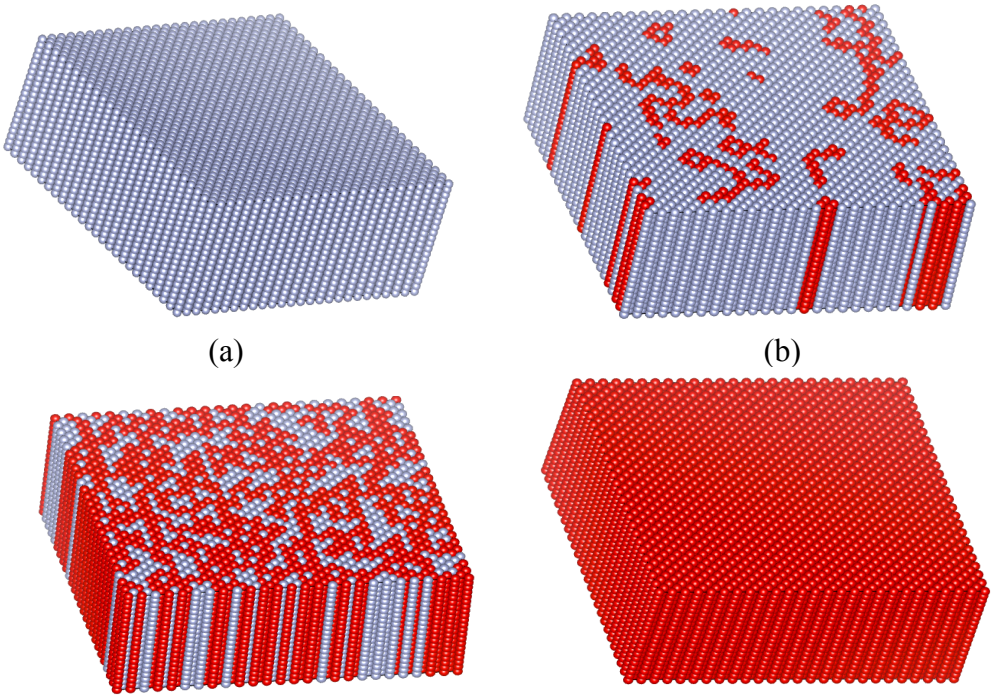

(a) (b)

(c) (d)

Figure 3.7: The spin structure of $CaMnFe_2O_6$ under external filed along reverse direction. Perovskite is ferromagnetic in (a) and (c) with reverse dipole direction. (c) and (d) show the columnar process of dipole direction change.

3.4.2 Origin of the displacement of coplanar Mn^{2+}

Mn^{2+} and Fe^{2+} have similar atomic radius and number of d electrons. Both experimental and computational studies show that they have distinct coordinate preference on the coplanar site. Coplanar Mn^{2+} has displacement along c-axis at any temperature, while coplanar Fe^{2+} stays perfectly inside the FeO_4 plane. Density functional theory calculations were used to explore the origin of coplanar displacement. Nonpolar C-type antiferromagnetic $CaMnTi_2O_6$ was simulated with symmetry constrain. The influence of coplanar displacement on d orbitals was investigated by analyzing density of states of each d orbital of polar and nonpolar phases. We found that the coplanar displacement can reduce the system energy of d^5 electronic configuration, while increase the system energy of d^6 electronic configuration.

The displacement of coplanar Mn^{2+} increases the distance between oxygen and manganese around coplanar site so as to stabilize the xy orbital. In density of states calculation shown in Figure 3.8, an energy drop of 0.1 eV is observed on the peak of the xy orbital, leading to a shift of Fermi level during the transition from nonpolar phase to polar phase. The displacement of coplanar Mn^{2+} compresses the z^2 orbital and increases its energy, shown in Figure 3.9. Density of states of the xz and yz orbitals are plotted in Figure 3.10. Based on crystal field theory, the xz and yz orbitals are equivalent for a coplanar coordinate environment, which agrees with our density of states calculation. Compared to the energy increment of z^2 orbital, relatively smaller energy increase is observed on the xz and yz orbitals. As is shown in Figure 3.11, the x^2-y^2 has no significant change during the nonpolar-polar phase transition. Energy change caused by the displacement of coplanar Mn^{2+} is plotted in Figure 3.12(a). The energy drop of the xy orbital is larger than the sum of

energy increase from the xz, yz and z^2 orbitals, resulting in a smaller system energy of $CaMnTi_2O_6$.

The coplanar Fe^{2+} has similar coordinate environment but has one more d electron compared to Mn^{2+}. Two states of the z^2 orbitals on coplanar Fe^{2+} are occupied. During the transition from nonpolar phase to polar phase, the energy of four electrons on the z^2, xz and yz orbitals will increase, while coplanar Mn^{2+} has only three electrons that increase in energy, shown in Figure 3.12(b). The amount of energy increase of electrons on the z^2, xz and yz orbitals is larger than the energy drop of electron from the xy orbital, resulting in a net increase of system energy. This d orbital density of states simulation explains why coplanar Fe^{2+} has no displacement from FeO_4 atomic plane. The density of states of z^2 orbitals of coplanar Fe^{2+} is plotted in Figure 3.13.

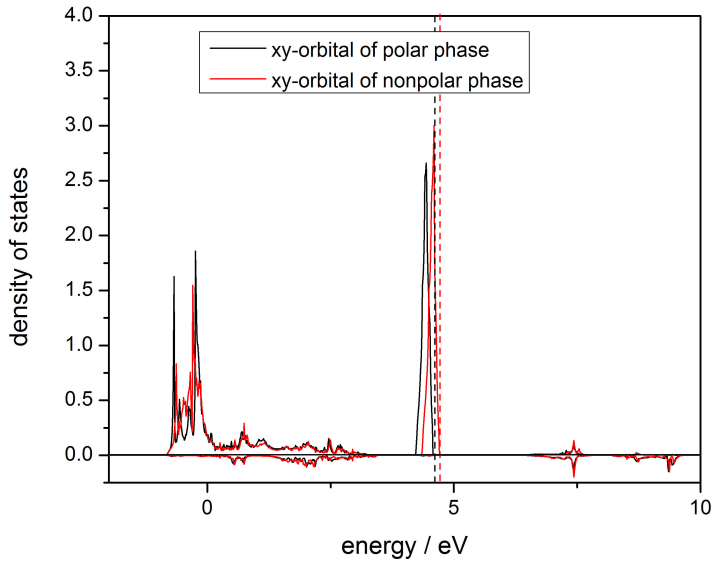

Figure 3.8: Density of states of the xy orbital of coplanar Mn^{2+} from polar and nonpolar phases. Fermi level is presented as dash line. The peak below Fermi level has an energy shift of 0.1 eV during the transition between polar and nonpolar phases.

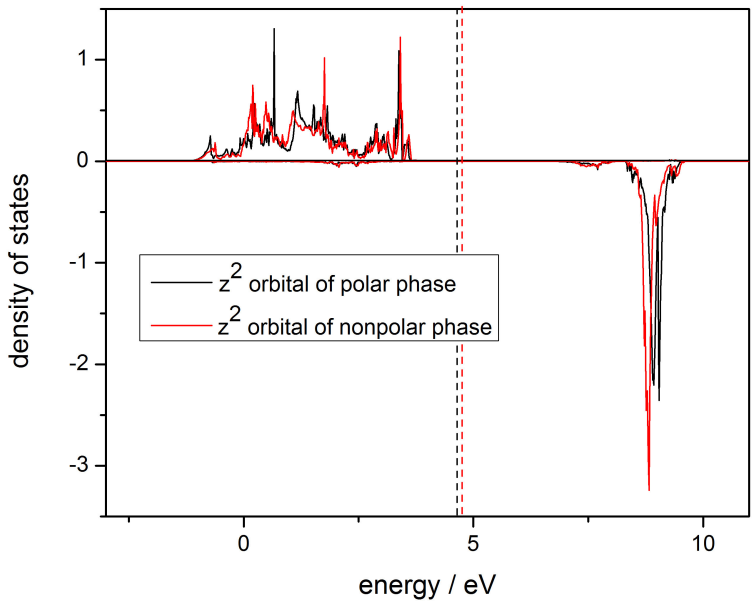

Figure 3.9: Density of states of the z^2 orbital of coplanar Mn^{2+} from polar and nonpolar phases. The z^2 orbital of polar phase is proved higher in energy through integration of occupied z^2 orbital. Fermi level is presented as dash line in the figure.

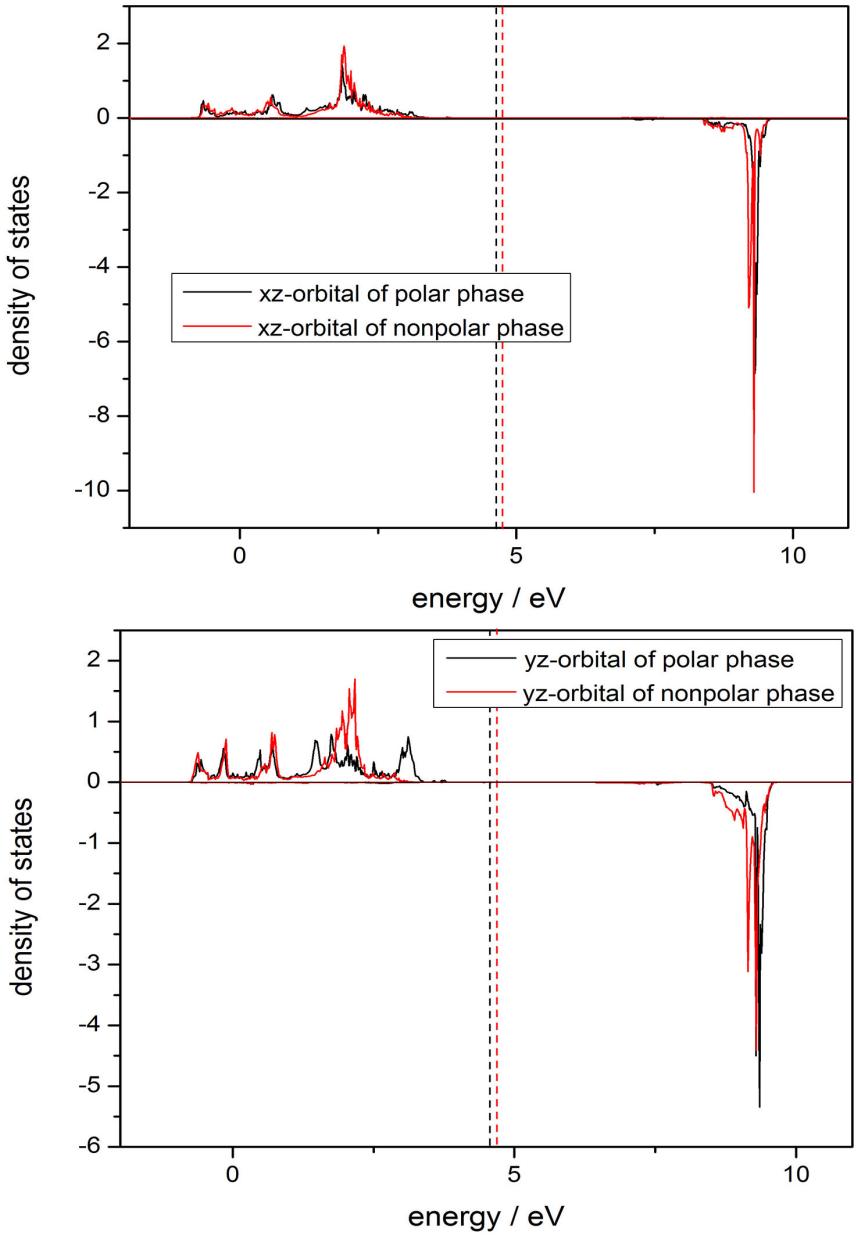

Figure 3.10: Density of states of the xz and yz orbitals of coplanar Mn^{2+} from polar and nonpolar phases. Fermi level is presented as dash line in the figure.

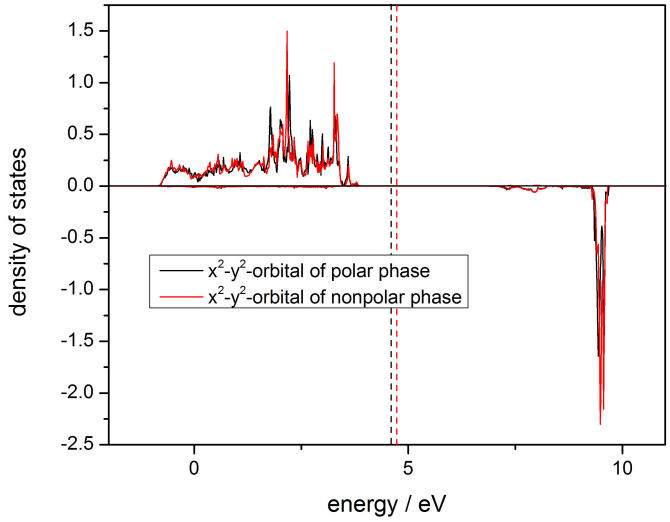

Figure 3.11: Density of states of the x^2-y^2 orbital from coplanar Mn^{2+} of polar and nonpolar phases. No significant energy change has been observed during the nonpolar-polar transition. Fermi level is presented as dash line in the figure.

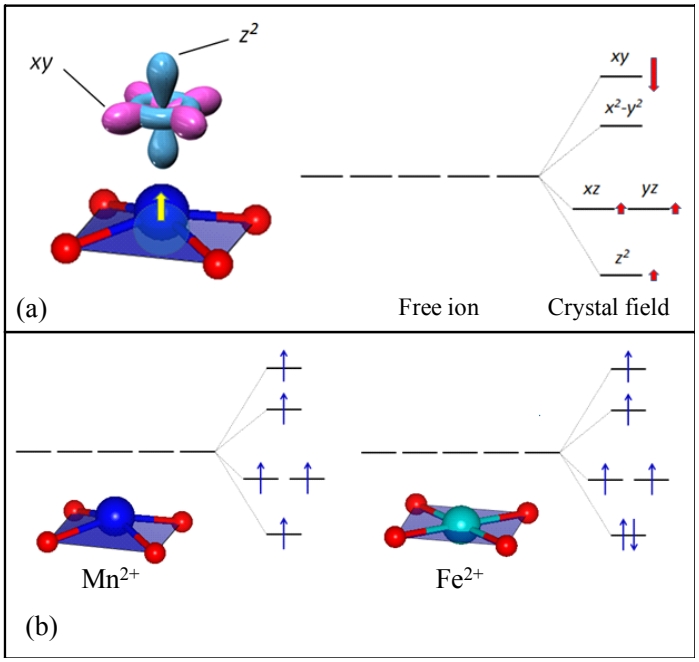

Figure 3.12: (a) D orbitals and displacement of coplanar Mn^{2+}. Red arrows show the energy change direction and amount of each orbital. (b) The orbital occupation of coplanar Mn^{2+} and Fe^{2+}. Blue arrows represent spins.[79]

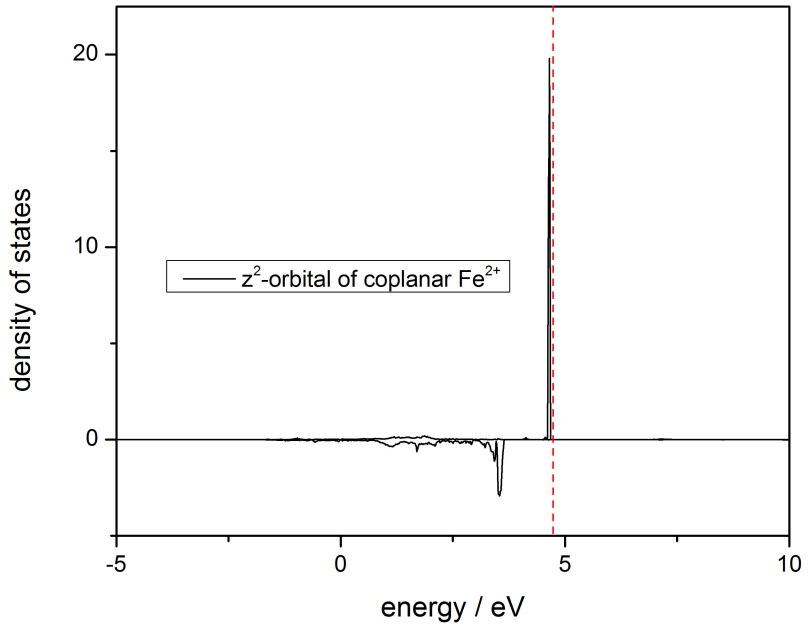

Figure 3.13: Density of states of the z^2 orbital of coplanar Fe^{2+}. Fe^{2+} has 6 d electrons and both spin-up and spin-down states of the z^2 orbital are occupied. Fermi level is presented as red dash line in the figure.

3.4.3 Origin of ferroelectricity

The coplanar MnO_4 has a rectangle shape in both polar and nonpolar phases. In high temperature nonpolar phase, the orientation of coplanar MnO_4 rectangle is random. As temperature decreases, the orientation of coplanar MnO_4 rectangle changes into ordered in the polar phase. In both polar and nonpolar phases, coplanar MnO_4 share oxygen with nearby octahedra. Orientation and displacement of coplanar MnO_4 will influence octahedral tilting. In nonpolar phase, the displacement of coplanar Mn^{2+} is random and local tilting pattern is a mixture of the $a^+b^+c^-$ and $b^+a^+c^-$.[79] This randomness lowers the symmetry of local coordinate environment and increases system's elastic energy, shown in Figure 3.14. At lower temperature, a better cooperativity between octahedral tilting and

coplanar MnO_4 is required to reduce system energy. As a result, the displacement of coplanar Mn^{2+} and orientation of coplanar MnO_4 rectangle must stay ordered to increase coordinate symmetry and reduce total energy. Our DFT simulation always produce a ground state of $P4_2mc$, which agrees with the ordered coplanar Mn^{2+} displacement at low temperature.

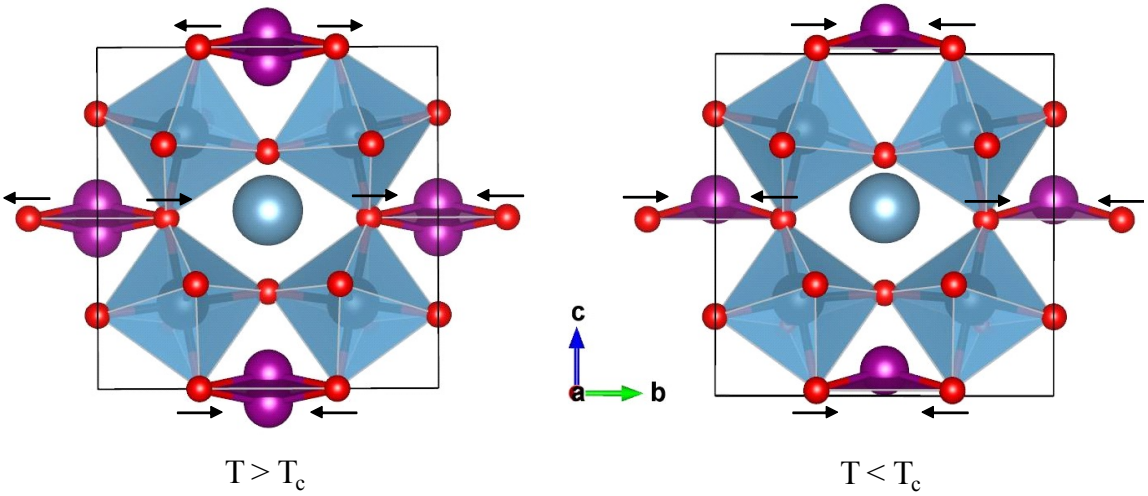

Figure 3.14: Displacement of coplanar Mn^{2+}, orientation of coplanar MnO_4 rectangle and cooperative octahedral tilting. Arrows indicate the direction of oxygen displacement associated with the rotation of MnO_4 plane. The disorder of the Mn^{2+} displacement direction and associated rectangle orientation at high temperature destroys the cooperativity of the octahedral network and increases the elastic energy the structure.[79]

3.4.4 Dipole moment analysis and enhancement

An explanation based on electronic structure analysis on the origin of coplanar displacement has been discussed. The displacement of coplanar Mn^{2+} lowers material's symmetry and causes distortion in TiO_6 octahedra and MnO_4 tetrahedra. I calculated the net dipole moment of the supercell plotted in Figure 3.2 and analyzed the contribution of coplanar, tetrahedral MnO_4 and TiO_6 octahedron

to the net dipole moment of the perovskite. A comparison between our simulation and experiment at 1.5K on net dipole moment components is illustrated in Table 3.6. Since ordered displacement of coplanar Mn^{2+} is critical in the formation of polar phase, we simulated similar double perovskite materials with different B-site atoms (Zr^{2+}, Sn^{2+} and Ge^{2+}) to find a material with larger net dipole moment. We discovered that $CaMnGe_2O_6$ has the largest coplanar displacement, smallest octahedral-site tilting and largest net dipole moment. The MnO_4 tetrahedra is quite stable and has no obvious change with different B-site atoms. The comparison on net dipole component and coplanar displacement between $CaMnGe_2O_6$ and $CaMnTi_2O_6$ is shown in Figure 3.15. The experiment to synthesize polar $CaMnGe_2O_6$ under high pressure and temperature is under the way.

Ferroelectricity of $CaMnTi_2O_6$ is correlated with the cooperative octahedral tilting, which can be easily influenced by epitaxial strain. We calculated the net dipole moment of $CaMnTi_2O_6$ under tensile and compressive epitaxial strain. We found that compressive strain can produce larger net dipole moment and a 1.5% compressive strain will enhance net dipole moment by 16.5%.

Table 3.6: Components of net dipole moment from simulation and experiment at 1.5 K

	Coplanar MnO_4	Tetrahedral MnO_4	Octahedral TiO_6
Experiment at 1.5 K	42%	5%	53%
DFT simulation	47%	5%	48%

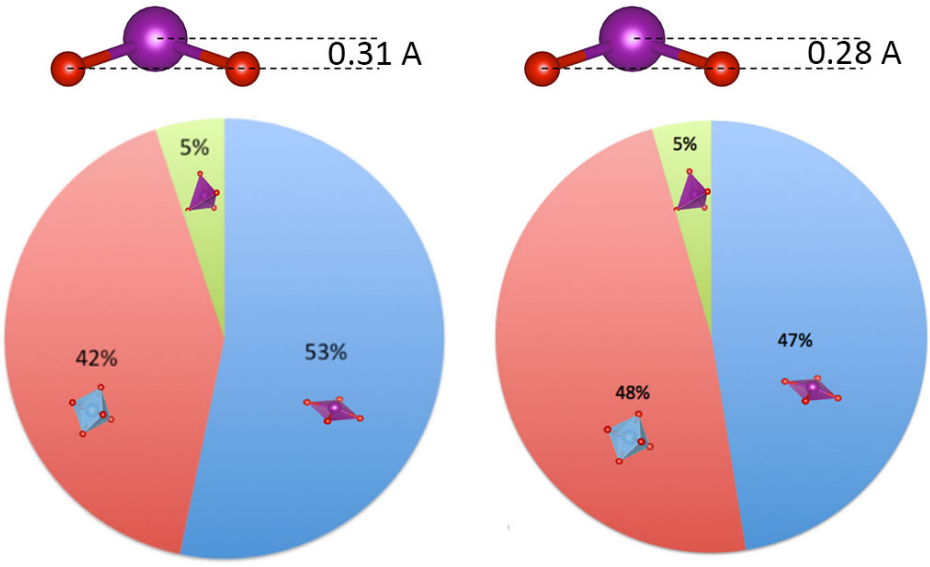

(a) $CaMnGe_2O_6$ (b) $CaMnTi_2O_6$

Figure 3.15: Displacement of coplanar Mn^{2+} and dipole component of $CaMnGe_2O_6$ and $CaMnTi_2O_6$. Compared to $CaMnTi_2O_6$, $CaMnGe_2O_6$ has larger coplanar displacement and less tilted octahedral network.

3.5 Conclusion

We discovered $CaMnTi_2O_6$ as a new type of ferroelectricity. Octahedral titling of perovskite generally produce nonpolar structure and proper ferroelectricity in the perovskites with octahedral-site tilting is rare. The ferroelectricity in $CaMnTi_2O_6$, similar to improper ferroelectricity, is caused by the order-disorder transition and related structural distortion. Even though the response of ferroelectricity in $CaMnTi_2O_6$ to depolarization field requires further exploration, our discovery provides a possible solution to the critical thickness problem in ferroelectric materials. Distortion at octahedral Ti^{4+}, coplanar and tetrahedral Mn^{2+} contribute to total ferroelectricity, which does not require soft polar mode from high symmetry phase. We also predicted several similar ferroelectric materials and

studied techniques to enhance ferroelectricity. The $CaMnTi_2O_6$ has a Curie temperature of 560 K. Our discovery provides a new direction for the design and search of ferroelectric perovskites.

3.6 Acknowledgement

I thank Zongyao Li for his guidance on experimental techniques employed in this $CaMnTi_2O_6$ research. I also thank Xiang Li for his inspiring introduction on $CaMnFe_2O_6$ perovskite. All our calculations are conducted on the facility of Texas Advanced Computing Center.

Chapter 4

Bulk modulus study on $CaCu_3B_4O_{12}$ perovskites

4.1 Abstract

We measured bulk modulus of several members from $CaCu_3B_4O_{12}$ family perovskites ($B = Ge, Mn, Cr, Ti, Ru$ and Ir) and found their bulk modulus violates Anderson's law, which states that there is a reverse relationship between volume and bulk modulus. Density functional theory simulations were conducted to calculate bulk modulus of $CaCu_3B_4O_{12}$ perovskites. Structures of $CaCu_3B_4O_{12}$ perovskites have been simulated and analyzed under pressure up to 15 GPa. We discovered that the $CaCu_3B_4O_{12}$ perovskites, even though they all adopt the same crystal structure, show different cooperative octahedral tilting behaviors under external pressure. Based on their octahedral tilting behaviors in response to external pressure, $CaCu_3B_4O_{12}$ perovskites have two mechanisms for the volume reduction in response to external pressure. In the 'octahedral shrinkage' mechanism, volume reduction is realized through compression of octahedral volume, generating a less tilted octahedral structure. In the 'octahedral tilting' mechanism, perovskites have more tilted octahedral network under pressure. Compression of octahedral volume is smaller in 'octahedral tilting' mechanism than that in 'octahedral shrinkage' mechanism. A more tilted octahedral structure generates larger bulk modulus, which leads to the violation of Anderson's law. More $CaCu_3B_4O_{12}$ perovskites were simulated through DFT calculations. We provided an explanation to the selection of volume reduction mechanism based on density of states analysis. Our

symmetry mode study established a linkage between Γ_2^+ octahedral rotation mode and perovskite's behavior under pressure.

4.2 Introduction

Bulk modulus describes how material's volume change in response to external pressure. A study of bulk modulus of perovskites can give us the equation of state, which is the essential input for the thermodynamic description of materials. Pressure has been widely employed in experiments and industry to change the lattice constant, octahedral tilting and many other structural deformations. The $CaCu_3B_4O_{12}$ family of perovskites have been widely studied during the last few decades because of their interesting electric and magnetic properties. $CaCu_3Ti_4O_{12}$ has a large dielectric constant over a wide temperature range.[31-34] $CaCu_3Mn_4O_{12}$ is a ferromagnetic semiconductor with a Curie temperature above room temperature.[35-36]

Six members of the $CaCu_3B_4O_{12}$ family of perovskites (B =Ge, Mn, Cr, Ti, Ru and Ir) were synthesized in our laboratory. All $CaCu_3B_4O_{12}$compounds adopt the A-site-ordered perovskite structure (space group $Im\bar{3}$), shown in Figure 4.1. The experimental result of the bulk modulus versus cell volume for $CaCu_3B_4O_{12}$ perovskites is plotted in Figure 4.2. We found that our six members from the $CaCu_3B_4O_{12}$ family perovskites can be divided into two groups: $CaCu_3Mn_4O_{12}$, $CaCu_3Ge_4O_{12}$ and $CaCu_3Cr_4O_{12}$ have a reverse relationship between volume and bulk modulus; while $CaCu_3Ti_4O_{12}$, $CaCu_3Ru_4O_{12}$ and $CaCu_3Ir_4O_{12}$'s bulk modulus increases with increasing volume. The second group attracted our interest due to its violation of Anderson's law. Anderson's law states that there is generally an inverse relationship between bulk modulus and volume.[84-85] Anderson's law has

been proved by many materials, typically, for materials with similar structures, larger volume indicates lower packing efficiency and smaller bulk modulus. The $CaCu_3B_4O_{12}$ family perovskites are interesting because only part of them follow Anderson's law. According to our experiments, the lattice constant difference between $CaCu_3Cr_4O_{12}$ and $CaCu_3Ti_4O_{12}$ is only 0.15 Å and both of them have the same cubic double perovskite structures. Our study was conducted to answer why materials in the same crystal structure show a different volume-bulk modulus relationship. Density functional theory calculations were employed to answer this question.

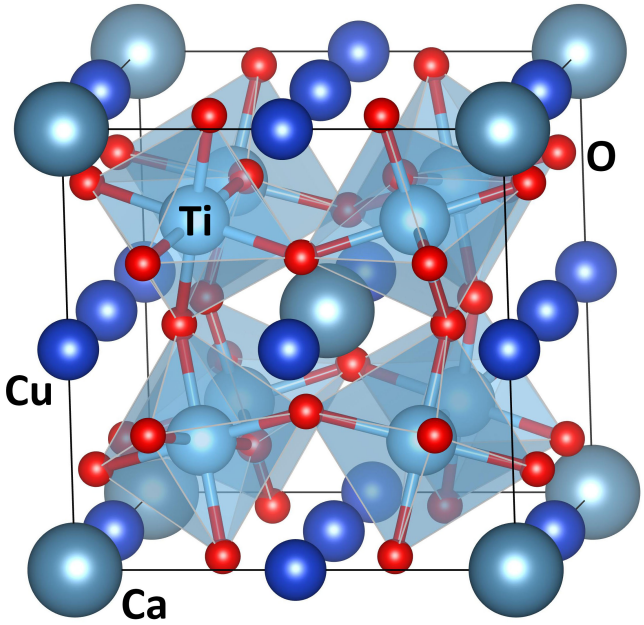

Figure 4.1: Structure of $CaCu_3Ti_4O_{12}$. All six perovskites synthesized in our study have the same cubic structure (space group #204). Octahedra form a three-dimensional tilted octahedral network through corner-sharing oxygen atoms.

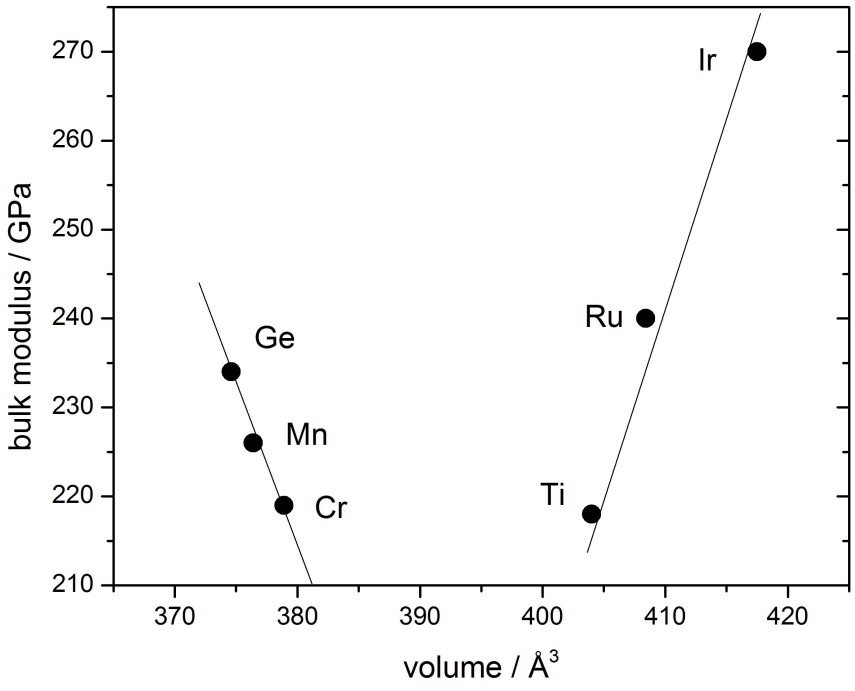

Figure 4.2: Relationship of $CaCu_3B_4O_{12}$ family perovskites between volume and bulk modulus.

4.3 Method

$CaCu_3Ge_4O_{12}$ was synthesized by mixing CaO, CuO and GeO_2 at 50-70 kbar and 1000 °C and by quenching to room pressure and temperature after 1 hour.[86] $CaCu_3Cr_4O_{12}$ was prepared by heating CaO, CuO and GrO_2 at 1100 °C and 6 kbar.[87] $CaCu_3Mn_4O_{12}$ was prepared by sintering $Ca(OH)_2$, CuO, MnO_2 and mixed with 15% $KClO_3$ at 1000 °C and 58 kbar for 30 min.[88] CaO, CuO and TiO_2 were mixed based on stoichiometric ratio and heated at 1000 °C for 12 hours to synthesize $CaCu_3Ti_4O_{12}$.[33] Polycrystalline $CaCu_3Ru_4O_{12}$ was synthesized by mixing and calcining $CaCO_3$, CuO and RuO_2 in air at 1050 °C for 20 hours.[89] $CaCu_3Ir_4O_{12}$ was prepared by mixing and heating $CaCO_3$, CuO and IrO_2 at 90 kbar

and 1300 °C for 30 min.[90] Bulk modulus is calculated by fitting the pressure dependence of cell volume to the Brich-Murnaghan (BM) equation.[91]

First-principle density functional theory calculations were performed on $CaCu_3B_4O_{12}$ family perovskites with the Vienna Ab Initio Simulation Package (VASP) and PBEsol+U functional.[58-59] Projected augmented wave (PAW) was selected in the simulation.[60] $CaCu_3B_4O_{12}$ perovskites with B = Ti, V, Cr, Mn, Fe, Co, Ni, Ge, Zr, Nb, Mo, Tc, Ru, Rh, Pd, Sn and Ir were simulated in our DFT calculations. All our simulations were conducted with symmetry constraints to keep all perovskites in the cubic structure (space group #204). The selection of the on-site Coulomb parameter U and exchange parameter J for the Cu atom are 5.0 eV and 1.0 eV. U and J for B-site atoms employed in the calculation are listed in Table 4.1. The selection of U and J can affect the material's simulated lattice constant. Our test calculations showed that the difference of bulk modulus caused by the selection of U and J can be as high as 10 to 15 GPa. However, no obvious change in pressure behavior has been observed. The selection of U and J are based on reported simulation of similar materials. For B-site atoms without clear information on U and J, parameters from neighbors in the periodic table were employed. Structural calculations were performed with 600 eV plane-wave cutoff and $6\times6\times6$ Monkhorst-Pack grid. A $15\times15\times15$ Monkhorst-Pack grid was employed in the density of states calculation to achieve higher accuracy. To study materials' structural response to external pressure, structures of all materials were simulated under pressure up to 15 GPa. Frozen phonon calculations were used to calculate the frequency and force constant of related octahedral tilting modes. Bulk modulus is calculated through the fitting of the volume-energy curve around lattice constant to

the Birch-Murnaghan equation.[92] An example of a bulk modulus calculation is shown in Figure 4.3.

Table 4.1: U and J parameters for B-site atoms

B-site atom	U / eV	J / eV
Ti	5.00	0.64
V	4.25	1.58
Cr	7.00	1.00
Mn	6.90	1.00
Fe	4.50	0.70
Co	4.30	1.00
Ni	4.50	1.00
Ge	0.00	0.00
Zr	3.00	1.50
Nb	3.00	1.50
Mo	3.70	1.90
Tc	2.50	1.50
Ru	2.50	1.00
Rh	2.50	1.00
Pd	2.50	1.00
Sn	0.00	0.00
Ir	2.50	1.00

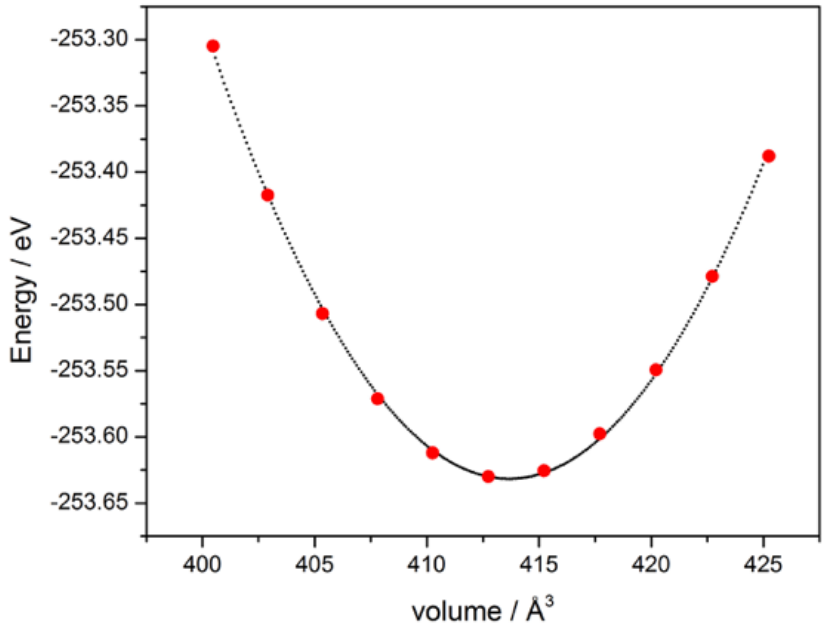

Figure 4.3: Simulated energy and corresponding volume of $CaCu_3Ir_4O_{12}$ (red dots). The black line is the fitted volume vs energy curve for bulk modulus calculation. $CaCu_3Ir_4O_{12}$ has a simulated lattice constant of 7.45 Å and bulk modulus of 245.7 GPa.

4.4 Results and discussion

The experimental and computational bulk modulus of $CaCu_3B_4O_{12}$ perovskites has been plotted in Figure 4.4. Our simulated bulk modulus agrees with experimental results. In simulation, the $CaCu_3B_4O_{12}$ family perovskites can still be separated into two groups. In most cases, our simulated bulk modulus is lower than the experimental bulk modulus. We calculated bulk modulus with different combinations of U and J and found that the choice of U and J can influence the value of the bulk modulus. This can become a possible explanation of the difference between computational and experimental bulk modulus. However, my simulation shows that the choice of U and J has no influence on how octahedron tilts and deforms under external pressure.

The influence of U on the volume and bulk modulus is a complex problem, which is highly dependent on the structure and electronic configuration for a given material. Here, I use my previous calculation on spinel materials as an example to illustrate the influence of U. In the calculation on ZnV_2O_4, I found that increasing the U value on Zn^{2+} leads to a smaller volume. However, a larger U on V^{3+} will increase the cell volume. In addition, larger U values on Zn^{2+} and V^{3+} reduces bulk modulus. It is not clear why larger U values have a different influence on volume but a similar influence on bulk modulus. Previous experience shows that LDA typically underestimate lattice constant and overestimate bulk modulus, while GGA overestimate lattice constant and underestimate bulk modulus. In another calculation on spinel MgV_2O_4, by changing U on V^{3+} from 2.7 eV to 5.3 eV, the lattice constant of MgV_2O_4 changes from 8.43 Å to 8.50 Å and its bulk modulus decreases by about 12 GPa. Similar to many perovskites, spinel structure also has both octahedral and tetrahedral sites, shown in Figure 4.5. The complex influence of U on volume and bulk modulus may result from the sensitivity to U on octahedral and tetrahedral sites.

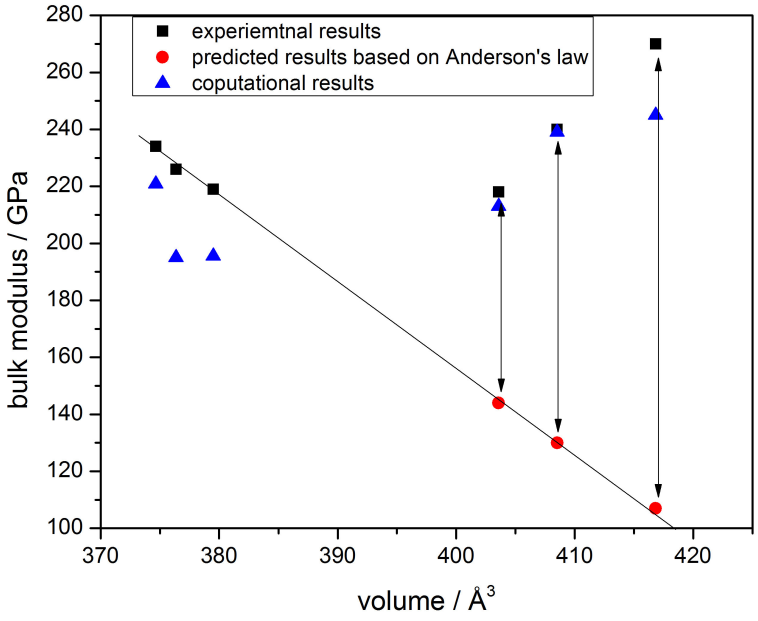

Figure 4.4: Experimental and computational bulk modulus. Anderson's law is plotted as a black solid line based on the volume vs. bulk modulus data of $CaCu_3Cr_4O_{12}$, $CaCu_3Mn_4O_{12}$ and $CaCu_3Ge_4O_{12}$. Predicted bulk modulus based on Anderson's law is relatively lower than experimental and simulated bulk modulus of $CaCu_3Ti_4O_{12}$, $CaCu_3Ru_4O_{12}$ and $CaCu_3Ir_4O_{12}$. The difference of bulk modulus between prediction of Anderson's law and experiments is believed to be caused by octahedral tilting, plotted as double arrows in the figure.

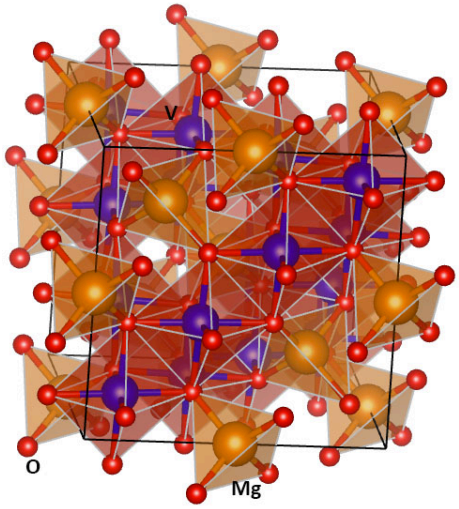

Figure 4.5: Structure of spinel MgV_2O_4. Mg2+ occupies tetrahedral site and V^{3+} occupies octahedral site. With increasing U on V^{3+} from 2.7 eV to 5.3 eV, the MgV_2O_4's bulk modulus changes from 175.7 GPa to 163.4 GPa.

We discovered that $CaCu_3B_4O_{12}$ perovskites can be divided into two groups based on their structural change under external pressure. For $CaCu_3Cr_4O_{12}$, $CaCu_3Mn_4O_{12}$ and $CaCu_3Ge_4O_{12}$, the B-O-B bond angle increases with increasing external pressure. In contrast, for $CaCu_3Ti_4O_{12}$, $CaCu_3Ru_4O_{12}$ and $CaCu_3Ir_4O_{12}$, the B-O-B bond angle has a reverse relationship with external pressure. The B-O-B bond angle is used to illustrate the amplitude of octahedral tilting, shown in Figure 4.6, and the relationship between pressure and B-O-B bond angle is plotted in Figure 4.7. Based on the relationship between octahedral tilting and external pressure, $CaCu_3B_4O_{12}$ perovskites behave differently under external pressure. The three-dimensional octahedral network of $CaCu_3Cr_4O_{12}$, $CaCu_3Mn_4O_{12}$ and $CaCu_3Ge_4O_{12}$ becomes less tilted with increasing external pressure. In contrast, external pressure produces a more tilted octahedral network in $CaCu_3Ti_4O_{12}$, $CaCu_3Ru_4O_{12}$ and $CaCu_3Ir_4O_{12}$.

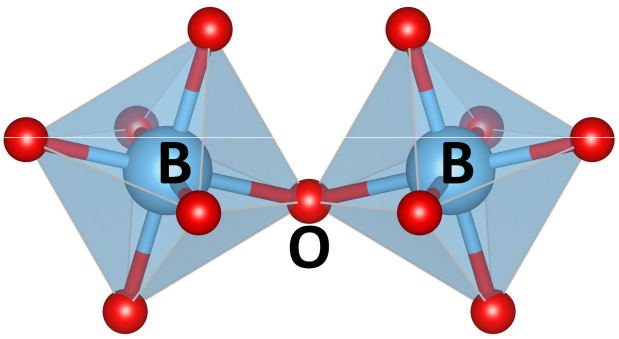

Figure 4.6: Graphic illustration of B-O-B bond angle. The B-O-B bond angle is employed to describe the amplitude of octahedral tilting in perovskite. A smaller B-O-B bond angle indicates a larger radius mismatch between A-site and B-site atoms and a more tilted octahedral structure.

The compressibility of the BO_6 octahedra is another important factor in the bulk modulus study of perovskite. Our calculations showed that the BO_6 octahedral volume of all $CaCu_3B_4O_{12}$ perovskites decreases under external pressure. According to Figure 4.8, the relationship between pressure and octahedral volume of $CaCu_3Cr_4O_{12}$, $CaCu_3Mn_4O_{12}$ and $CaCu_3Ge_4O_{12}$ has a more negative slope than $CaCu_3Ti_4O_{12}$, $CaCu_3Ru_4O_{12}$ and $CaCu_3Ir_4O_{12}$. The more negative slope indicates that $CaCu_3Cr_4O_{12}$, $CaCu_3Mn_4O_{12}$ and $CaCu_3Ge_4O_{12}$ have softer BO_6 octahedra than that in $CaCu_3Ti_4O_{12}$, $CaCu_3Ru_4O_{12}$ and $CaCu_3Ir_4O_{12}$.

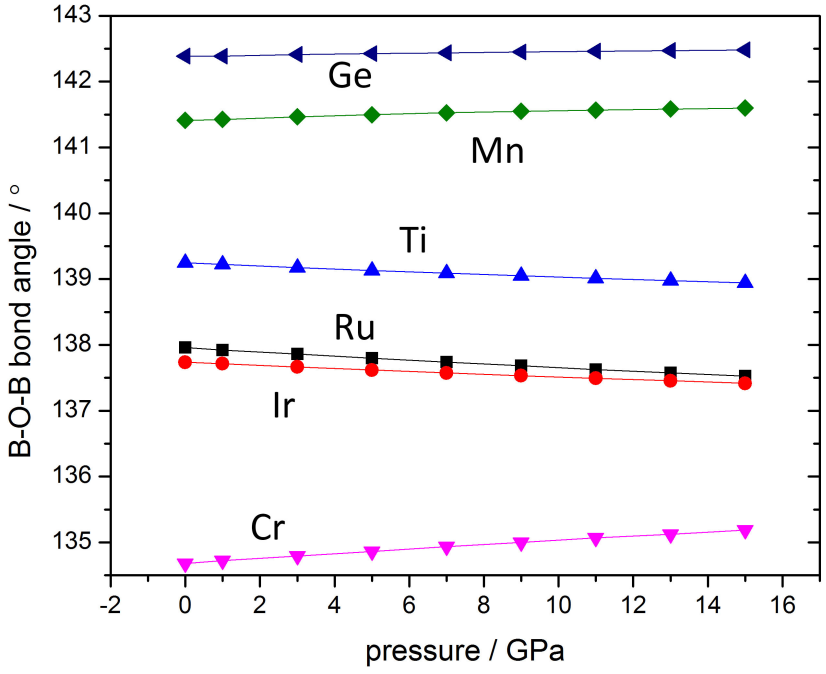

Figure 4.7: The relationship between B-O-B bond angle and pressure of $CaCu_3B_4O_{12}$ perovskites. The relationship between B-O-B bond angle and pressure of $CaCu_3Cr_4O_{12}$, $CaCu_3Mn_4O_{12}$ and $CaCu_3Ge_4O_{12}$ has a positive slope, indicating a less tilted octahedral structure under higher pressure. The reverse relationship of $CaCu_3Ti_4O_{12}$, $CaCu_3Ru_4O_{12}$ and $CaCu_3Ir_4O_{12}$ between B-O-B bond angle and pressure shows that a more titled structure is generated under high pressure.

The change of tilting angle and octahedral volume with external pressure indicates two competing mechanisms of the cell volume reduction under pressure. In the mechanism observed on $CaCu_3Cr_4O_{12}$, $CaCu_3Mn_4O_{12}$ and $CaCu_3Ge_4O_{12}$ (called 'octahedral shrinkage' mechanism), the volume reduction under pressure is realized by the shrinkage of softer BO_6 octahedra, resulting in a larger B-O-B bond angle and less tilted structure. In the other mechanism observed on $CaCu_3Ti_4O_{12}$, $CaCu_3Ru_4O_{12}$ and $CaCu_3Ir_4O_{12}$ (called 'octahedral tilting' mechanism), external pressure results in a more tilted octahedral network. The more tilted octahedral network improves perovskite's space efficiency and reduces total volume. Previous study on physical properties of perovskite shows that perovskite with a more tilted octahedral structure will have a more densely packed structure and larger bulk modulus. As a result, the more tilted structure generated in the 'octahedral tilting' mechanism will produce a larger bulk modulus. This explains why bulk modulus increases when B-site atom changes to Ti, Ru and Ir. Among $CaCu_3Ti_4O_{12}$, $CaCu_3Ru_4O_{12}$ and $CaCu_3Ir_4O_{12}$, $CaCu_3Ir_4O_{12}$ has the smallest B-O-B bond angle and most tilted octahedral network. The 'octahedral tilting' mechanism will give $CaCu_3Ir_4O_{12}$ the most tilted structure and largest bulk modulus, which agrees with our experimental observation. If all $CaCu_3B_4O_{12}$ perovskites followed the 'octahedral shrinkage' mechanism under external pressure, the bulk modulus of $CaCu_3B_4O_{12}$ family perovskites would comply with Anderson's law and $CaCu_3Ir_4O_{12}$ would have the smallest bulk modulus of these six $CaCu_3B_4O_{12}$ perovskites. However, the 'octahedral tilting' mechanism on $CaCu_3Ti_4O_{12}$, $CaCu_3Ru_4O_{12}$ and $CaCu_3Ir_4O_{12}$ produces more tilted structures and larger bulk modulus. The differences between predicted bulk modulus based on Anderson's

law and experimental bulk modulus of $CaCu_3Ti_4O_{12}$, $CaCu_3Ru_4O_{12}$ and $CaCu_3Ir_4O_{12}$ are shown in Figure 4.4.

The origin of these two cell volume reduction mechanisms is an interesting research topic. To investigate which factor plays the role in selecting these two volume reduction mechanisms for a perovskite, more 3d and 4d transition metals were tested as B-site atoms in our DFT calculations. Structural behavior under pressure of our simulated $CaCu_3B_4O_{12}$ perovskites is shown is Figure 4.9. For 3d B-site atoms, the boundary between these two mechanisms is between vanadium and chromium. As for 4d B-site atoms, only $CaCu_3Pd_4O_{12}$ reduces volume under external pressure through 'octahedral shrinkage' mechanism. Our calculation shows that $CaCu_3Ru_4O_{12}$ perovskites that are close in volume and electronic structure can have distinct octahedral rotation behaviors under pressure. The change of tilting angle with pressure is a significant indicator in our analysis. According to Figure 4.7, the B-O-B bond angle of $CaCu_3Ti_4O_{12}$, $CaCu_3Ru_4O_{12}$ and $CaCu_3Ir_4O_{12}$ is larger than that of $CaCu_3Cr_4O_{12}$ and smaller than the B-O-B bond angle of $CaCu_3Mn_4O_{12}$. As a result, the absolute value of octahedral tilting angle is not a critical factor.

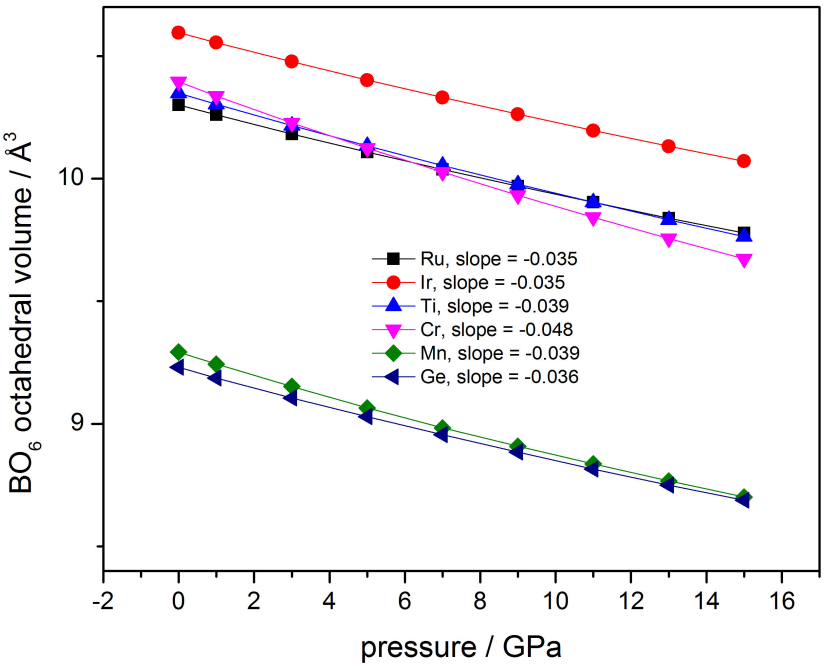

Figure 4.8: The relationship between pressure and BO_6 octahedral volume. Octahedral volume of all materials is compressed under pressure. The softer octahedra of $CaCu_3Cr_4O_{12}$, $CaCu_3Mn_4O_{12}$ and $CaCu_3Ge_4O_{12}$ is proved by their more negative slopes.

We calculated the density of states of the $CaCu_3B_4O_{12}$ family perovskites. Our calculation shows that the compression of BO_6 octahdedra will broaden d orbitals of B-site atoms. The d orbital densities of states of $CaCu_3V_4O_{12}$ and $CaCu_3Fe_4O_{12}$ are plotted in Figure 4.10. Integration was conducted on occupied d orbitals of vanadium and iron atoms. We found that external pressure increases the energy of d orbital in both materials. For $CaCu_3V_4O_{12}$, the energy of d orbital of vanadium atom increases by 0.04 eV at 7 GPa and 0.08 eV at 15 GPa. For $CaCu_3Fe_4O_{12}$, the energy of d orbital of iron increases by 0.03 eV at 7 GPa and 0.07 eV at 15 GPa. The compression of BO_6 octahdedra not only broadens d orbitals, but also increases the energy of d orbitals. When number of d electrons is

small, the energy increment caused by octahedral volume compression is small because most d orbitals are unoccupied. So 'octahedral shrinkage' mechanism should be energetically more favorable than 'octahedral tilting' mechanism for materials with only a few d electrons. When B-site atoms have more d electrons, most d orbitals will be occupied and octahedral shrinkage will cause much larger energy increase, leading to a harder octahedron. This conclusion agrees with my simulation that more 4d perovskites choose 'octahedral tilting' mechanism than 3d perovskites. However, Ni^{4+}, Co^{4+} and Fe^{4+}, which have more d electrons than Ti^{4+} and V^{4+}, choose 'octahedral shrinkage' mechanism, indicating they have a softer BO_6 octahedron. This contradicts with the conclusion that octahedron is harder when there are more d electrons, indicating that more factors are required in the bulk modulus investigation.

The conclusion that materials with larger number of d electrons are harder agrees with our experience in many cases. 5d-electron materials are usually harder than 4d and 3d-electron materials. For example, osmium has been reported a large bulk modulus of 462 GPa.[93] However, many materials violate this conclusion. Diamond has a bulk modulus of more than 440 GPa.[94-95] Iridium, which has one more d electron than osmium, has a much lower bulk modulus of 320 GPa. Bulk modulus can be affected by many factors, such as symmetry and bond type.[96] Number of d electrons is one factor in the determination of bulk modulus, but not always a significant factor. When comparing bulk modulus of materials with similar symmetry and bonds, number of d electrons can become an important consideration in the bulk modulus study.

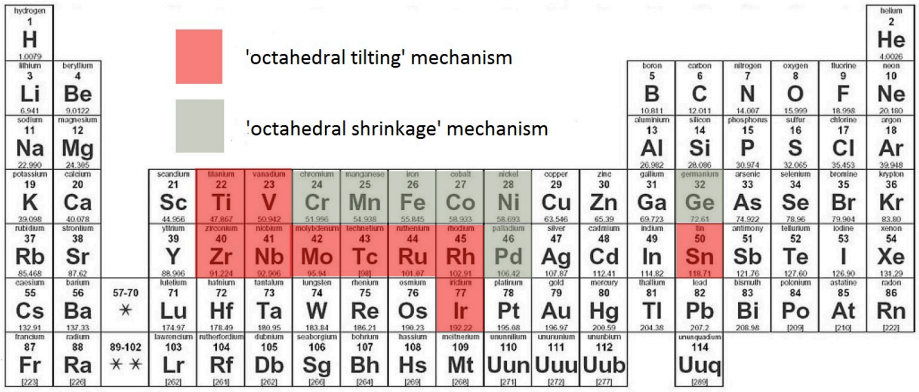

Figure 4.9: Volume reduction mechanisms of $CaCu_3B_4O_{12}$ perovskites. Most 3d B-site atom materials follow the 'octahedral shrinkage' mechanism. The boundary between two mechanisms is between vanadium and chromium. Most 4d B-site atom materials, except for $CaCu_3Pd_4O_{12}$, reduce volume through the 'octahedral tilting' mechanism.

We analyzed $CaCu_3B_4O_{12}$ perovskites' behavior under pressure using a symmetry mode approach. The Γ_2^+ octahedral rotation mode from $CaCu_3B_4O_{12}$ perovskite's high symmetry phase (space group $Im\bar{3}m$) can be used to describe the octahedral tilting behavior in 'octahedral tilting' mechanism. $CaCu_3B_4O_{12}$ perovskites experience Γ_2^+ octahedral rotation during the transition from high symmetry $Im\bar{3}m$ phase to $Im\bar{3}$ phase, shown in Figure 4.11. Force constant of Γ_2^+ octahedral rotation mode from parent phase is used to describe the softness of this rotation mode. A negative force constant indicates the existence of positive driving force of specific octahedral rotation mode. I calculated the force constant and phonon frequency of Γ_2^+ mode of all $CaCu_3B_4O_{12}$ perovskites. Their Γ_2^+ force constant are listed in Table 4.2. All $CaCu_3B_4O_{12}$ perovskites have negative Γ_2^+ force constant and imaginary Γ_2^+ phonon frequency, indicating that the Γ_2^+ octahedral rotation is energetically favorable in high symmetry phase. We found that $CaCu_3B_4O_{12}$ perovskites' choice on volume reduction mechanism is associated

with the Γ_2^+ force constant of high symmetry phase. Materials of 'octahedral tilting' mechanism typically have very large negative Γ_2^+ force constant. In contrast, Materials of 'octahedral shrinkage' mechanism usually have Γ_2^+ force constant force constant between -5 and 0 eV/Å^2. Large gap of Γ_2^+ force constant has been observed at the boundary between these two groups of $CaCu_3B_4O_{12}$ perovskites. For materials with 3d B-site atoms, when B-site atom change from vanadium to chromium, the Γ_2^+ force constant jumps from -4.01 to -10.1 eV/Å^2. As for materials with 4d B-site atoms, $CaCu_3Pd_4O_{12}$ has a Γ_2^+ force constant of -7.57 eV/ Å^2, which is more negative than other $CaCu_3B_4O_{12}$ perovskites containing 4d B-site atoms.

The explanation of the association between Γ_2^+ symmetry mode and the behavior under pressure is challenging because a more negative Γ_2^+ force constant means that the Γ_2^+ octahedral rotation mode is softer in high symmetry phase and more easily to generate a tilted structure during phase transition. However, these perovskites will compress the octahedral volume and produce a less tilted structure under external pressure. The imaginary Γ_2^+ phonon frequency and negative Γ_2^+ force constant reveal the double well energy surface in high symmetry phase, shown in Figure 4.12. The relative amplitude of Γ_2^+ octahedral rotation can be described with the value of Γ_2^+ force constant. A more negative Γ_2^+ force constant indicates that the material will have relatively larger Γ_2^+ octahedral rotation during the transition from high symmetry $Im\bar{3}m$ phase to $Im\bar{3}$ phase. When they are in $Im\bar{3}$ phase, perovskites with more negative Γ_2^+ force constant are more stable to Γ_2^+ octahedral rotation because more Γ_2^+ octahedral rotation potential has been exhausted during phase transition. As a result, when external pressure is applied, perovskites, whose parent phase has a more negative Γ_2^+ force constant, will not choose the more stable

Γ_2^+ octahedral rotation; they compress the octahedral volume and produce a less tilted octahedral network.

Table 4.2: Γ_2^+ force constant of $CaCu_3B_4O_{12}$ perovskites in space group $Im\bar{3}m$

Material	Γ_2^+ force constant / eV/ Å^2	Volume reduction mechanism
$CaCu_3Cr_4O_{12}$	-10.10	'octahedral titling' mechanism
$CaCu_3FeO_{12}$	-5.10	
$CaCu_3Ge_4O_{12}$	-7.29	
$CaCu_3Pd_4O_{12}$	-7.57	
$CaCu_3Ti_4O_{12}$	-4.68	'octahedral shrinkage' mechanism
$CaCu_3V_4O_{12}$	-4.02	
$CaCu_3Zr_4O_{12}$	-3.02	
$CaCu_3Nb_4O_{12}$	-2.84	
$CaCu_3Mo_4O_{12}$	-2.61	
$CaCu_3Tc_4O_{12}$	-2.81	
$CaCu_3Ru_4O_{12}$	-5.17	
$CaCu_3Rh_4O_{12}$	-4.68	
$CaCu_3Sn_4O_{12}$	-7.57	
$CaCu_3Ir_4O_{12}$	-4.66	

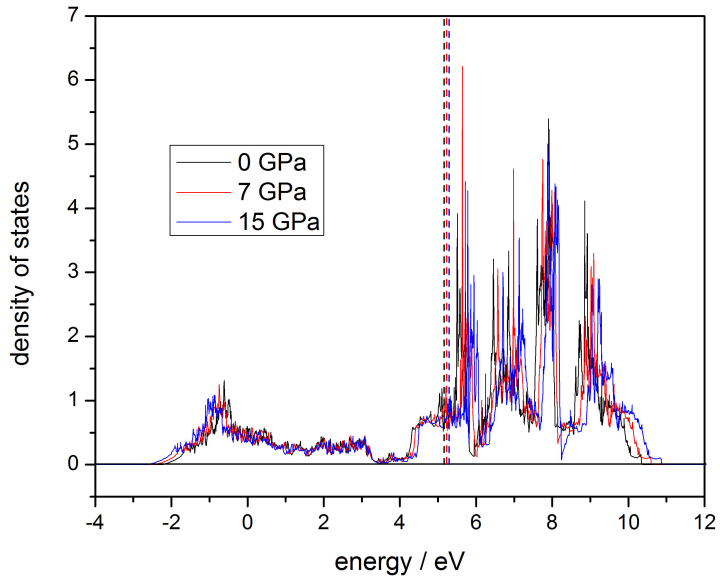

(a)

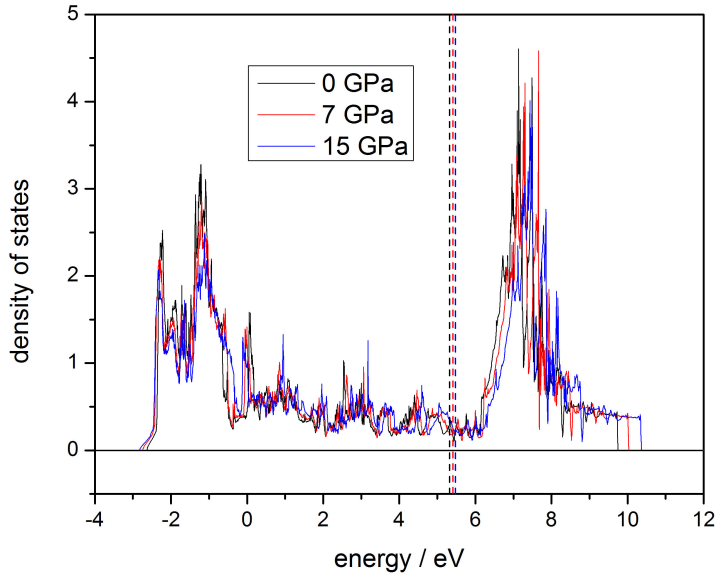

(b)

Figure 4.10: Density of states of B-site atom's d orbital of $CaCu_3V_4O_{12}$ (a) and $CaCu_3Fe_4O_{12}$ (b) under pressure. Fermi level is plotted as dash line. $CaCu_3V_4O$ and $CaCu_3Fe_4O_{12}$ have different volume reduction mechanisms under pressure. However, there is no obvious difference between their density of states. BO_6 ocathedra are compressed in both mechanisms, resulting in broader d orbitals.

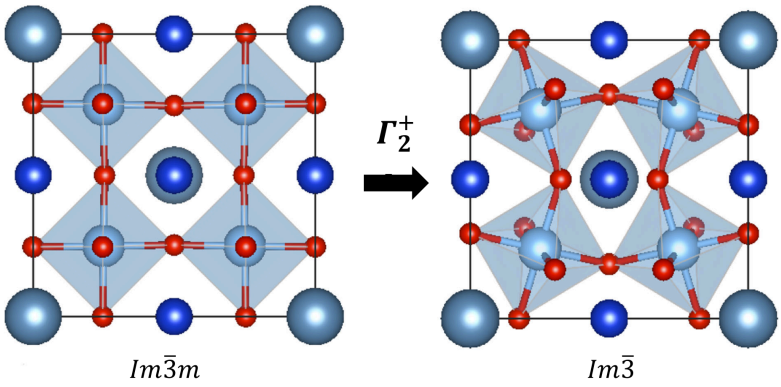

Figure 4.11: $CaCu_3V_4O_{12}$ perovskites experience Γ_2^+ octahedral rotation mode during its phase transition between space group $Im\bar{3}m$ and $Im\bar{3}$. Γ_2^+ octahedral rotation mode lowers perovskite symmetry by generating a titled octahedral network.

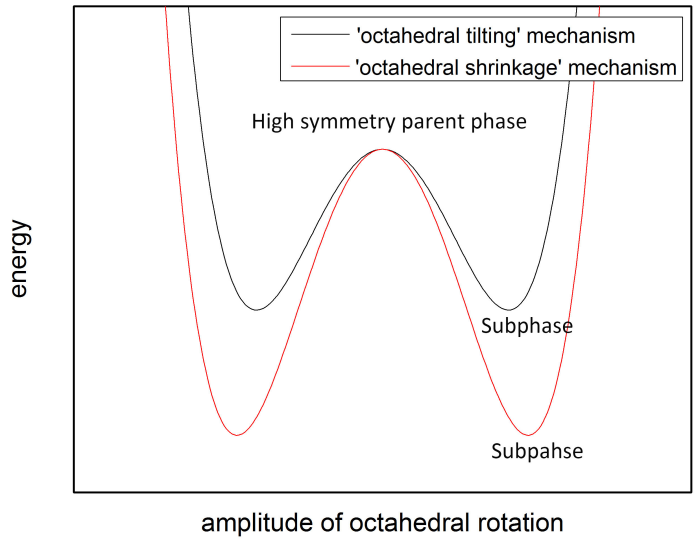

Figure 4.12: Double well energy surface of high symmetry parent phase. Octahedral rotation along Γ_2^+ mode will lower the symmetry of parent phase and reduce parent phase's energy. Materials of 'octahedral shrinkage' mechanism experience relatively larger Γ_2^+ octahedral rotation during the phase transition between parent phase and subphase. The subphase's potential of Γ_2^+ octahedral rotation is exhausted during phase transition. So, subpahses of 'octahedral shrinkage' mechanism is insensitive to Γ_2^+ octahedral rotation and compress its octahedral volume under pressure.

My study indicates that multiple factors have influence on the structural change of $CaCu_3B_4O_{12}$ perovskites under pressure. To obtain a direct comparison between octahedral compression and tilting, all displacement modes are calculated and analyzed through phonon calculation. No displacement mode solely corresponding to octahedral compression is discovered. Due to the corner-sharing octahedral structure, octahedral compression and tilting are correlated in displacement mode. Any change in the amplitude of displacement mode will change octahedral volume and tilting simultaneously. The 'octahedral shrinkage' and 'octahedral tilting' mechanisms follow the same displacement mode but along reverse directions. Energy surfaces of $CaCu_3Ti_4O_{12}$ and $CaCu_3Ge_4O_{12}$ are plotted in Figure 4.13. Under external pressure, the amplitude change of Γ_2^+ displacement mode is determined by the slope of energy surface. A smaller energy surface slope is energetically favorable under pressure because the lower energy increase at the same amplitude change of displacement mode. $CaCu_3Ti_4O_{12}$, as an example of the 'octahedral tilting' group, has an increase in the amplitude of Γ_2^+ displacement mode during the structural change under pressure. The 'octahedral shrinkage' group has a lower amplitude of Γ_2^+ displacement mode during the structural change under pressure, resulting in a less tilted structure.

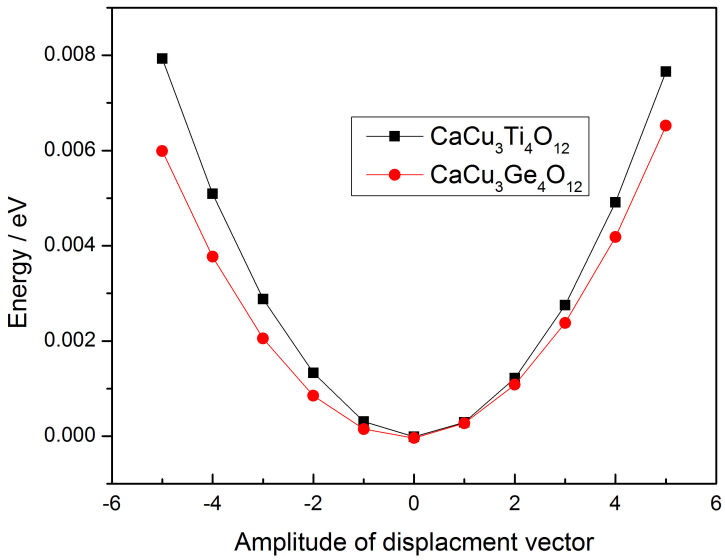

Figure 4.13: Energy surface of $CaCu_3B_4O_{12}$ and $CaCu_3B_4O_{12}$ as a function of the amplitude of Γ_2^+ displacement vector.

4.5 Conclusion

By measuring the bulk modulus of $CaCu_3B_4O_{12}$ perovskites, we found that the volume-bulk modulus relation of $CaCu_3B_4O_{12}$ perovskites with B = Ti, Cr, Mn, Ge, Ru and Ir does not comply with Anderson's law. A few $CaCu_3B_4O_{12}$ perovskites' bulk modulus increases with the increment of volume. DFT calculations were conducted to calculate materials' bulk modulus and simulate perovskite's behavior under external pressure. We discovered that $CaCu_3B_4O_{12}$ perovskites can be divided into two groups based on their volume reduction mechanisms. As the cell volume reduces, $CaCu_3Cr_4O_{12}$, $CaCu_3Mn_4O_{12}$ and $CaCu_3Ge_4O_{12}$ choose to have their octahedral volume reduced, resulting in a less tilted structure. In contrast, $CaCu_3Ti_4O_{12}$, $CaCu_3Ru_4O_{12}$ and $CaCu_3Ir_4O_{12}$ have a more tilted structure under external pressure. The more tilted structure increases the packing efficiency and therefore the bulk modulus. The compression of octahedral volume is relatively smaller in $CaCu_3Ti_4O_{12}$, $CaCu_3Ru_4O_{12}$ and $CaCu_3Ir_4O_{12}$.

Through orbital analysis, we explained why ‘octahedral shrinkage’ mechanism is preferred when B-site atom has only a few d electrons. Compression of octahedral volume will broaden d orbitals and increase orbital energy. Large number of d electrons leads to larger energy increase during octahedral compression, producing a harder BO_6 octahedron. At last, we established a linkage between the Γ_2^+ force constant of high symmetry phase and perovskite’s volume reduction mechanism.

Bibliography

1. Green, M. A.; Ho-Baillie, A.; Snaith, H. J., The emergence of perovskite solar cells. Nature Photonics 2014, 8, 506.
2. Bonanos, N.; Knight, K. S.; Ellis, B., Perovskite solid electrolytes: Structure, transport properties and fuel cell applications. Solid State Ionics 1995, 79, 161-170.
3. Yang, G.; Su, C.; Ran, R.; Tade, M. O.; Shao, Z., Advanced Symmetric Solid Oxide Fuel Cell with an Infiltrated K_2NiF_4-Type La_2NiO_4 Electrode. Energy & Fuels 2014, 28 (1), 356-362.
4. Egger, A.; Schrödl, N.; Gspan, C.; Sitte, W., $La_2NiO_{4+\delta}$ as electrode material for solid oxide fuel cells and electrolyzer cells. Solid State Ionics 2017, 299, 18-25.
5. Liu, M.; Johnston, M. B.; Snaith, H. J., Efficient planar heterojunction perovskite solar cells by vapour deposition. Nature 2013, 501, 395.
6. Hinks, D. G.; Dabrowski, B.; Jorgensen, J. D.; Mitchell, A. W.; Richards, D. R.; Pei, S.; Shi, D., Synthesis, structure and superconductivity in the $Ba_{1-x}K_xBiO_{3-y}$ system. Nature 1988, 333, 836.
7. Cao, G.; Qi, T. F.; Li, L.; Terzic, J.; Yuan, S. J.; DeLong, L. E.; Murthy, G.; Kaul, R. K., Novel Magnetism of $Ir^{5+}(5d^4)$ Ions in the Double Perovskite Sr_2YIrO_6. Physical Review Letters 2014, 112 (5), 056402.
8. Scott, J. F.; Dawber, M., Oxygen-vacancy ordering as a fatigue mechanism in perovskite ferroelectrics. Applied Physics Letters 2000, 76 (25), 3801-3803.
9. Wu, Y.; Cao, G., Enhanced ferroelectric properties and lowered processing temperatures of strontium bismuth niobates with vanadium doping. Applied Physics Letters 1999, 75 (17), 2650-2652.
10. Goodenough, J. B.; kafalas, J. A., Exploring the $A^+B^{5+}O_3$ compounds. Journal of Solid State Chemistry 1973, 6 (4), 493-501.
11. Yagi, T.; Mao, H.-K.; Bell, P. M., Structure and crystal chemistry of perovskite-type MgSiO3. Physics and Chemistry of Minerals 1978, 3 (2), 97-110.
12. M Woodwardt, P., Octahedral Tilting in Perovskites. I. Geometrical Considerations. Acta Crystallographica Section B 1997, Vol. 53, 32-43.
13. Chandran, P. R.; Arjunan, T. V., A Review of Materials used for Solid Oxide Fuel Cell.
14. Minh, N. Q.; Takahashi, T., Science and technology of ceramic fuel cells. Elsevier: 1995.
15. Liu, J.; Barnett, S. A., Operation of anode-supported solid oxide fuel cells on methane and natural gas. Solid State Ionics 2003, 158 (1), 11-16.

16. Ullmann, H.; Trofimenko, N.; Tietz, F.; Stöver, D.; Ahmad-Khanlou, A., Correlation between thermal expansion and oxide ion transport in mixed conducting perovskite-type oxides for SOFC cathodes. Solid State Ionics 2000, 138 (1), 79-90.

17. Sengodan, S.; Choi, S.; Jun, A.; Shin, T. H.; Ju, Y.-W.; Jeong, H. Y.; Shin, J.; Irvine, J. T. S.; Kim, G., Layered oxygen-deficient double perovskite as an efficient and stable anode for direct hydrocarbon solid oxide fuel cells. Nature Materials 2014, 14, 205.

18. Acres, G. J. K.; Frost, J. C.; Hards, G. A.; Potter, R. J.; Ralph, T. R.; Thompsett, D.; Burstein, G. T.; Hutchings, G. J., Electrocatalysts for fuel cells. Catalysis Today 1997, 38 (4), 393-400.

19. Dicks, A. L., Advances in catalysts for internal reforming in high temperature fuel cells. Journal of Power Sources 1998, 71 (1), 111-122.

20. Gholamian, E.; Zare, V., A comparative thermodynamic investigation with environmental analysis of SOFC waste heat to power conversion employing Kalina and Organic Rankine Cycles. Energy Conversion and Management 2016, 117, 150-161.

21. Singhal, S. C., Solid oxide fuel cells for stationary, mobile, and military applications. Solid State Ionics 2002, 152-153, 405-410.

22. Chen, G.; Kishimoto, H.; Yamaji, K.; Kuramoto, K.; Horita, T., Electrical Performance of La-Substituted $SrTiO_3$ Anode Material with Different Deficiency in A-Site. ECS Transactions 2013, 50 (27), 63-71.

23. Cain, T. A.; Kajdos, A. P.; Stemmer, S., La-doped $SrTiO_3$ films with large cryogenic thermoelectric power factors. Applied Physics Letters 2013, 102 (18), 182101.

24. Yan, L.; Yang, Y.; Wang, Z.; Xing, Z.; Li, J.; Viehland, D., Review of magnetoelectric perovskite–spinel self-assembled nano-composite thin films. Journal of Materials Science 2009, 44 (19), 5080-5094.

25. Choi, K. J.; Biegalski, M.; Li, Y. L.; Sharan, A.; Schubert, J.; Uecker, R.; Reiche, P.; Chen, Y. B.; Pan, X. Q.; Gopalan, V.; Chen, L.-Q.; Schlom, D. G.; Eom, C. B., Enhancement of Ferroelectricity in Strained $BaTiO_3$ Thin Films. Science 2004, 306 (5698), 1005-1009.

26. Specht, E. D.; Christen, H. M.; Norton, D. P.; Boatner, L. A., X-Ray Diffraction Measurement of the Effect of Layer Thickness on the Ferroelectric Transition in Epitaxial $KTaO_3/KNbO_3$ Multilayers. Physical Review Letters 1998, 80 (19), 4317-4320.

27. Naoko Yanase; Kazuhide Abe; Noburu Fukushima; Takashi Kawakubo, Thickness Dependence of Ferroelectricity in Heteroepitaxial $BaTiO_3$ Thin Film Capacitors. Japanese Journal of Applied Physics 1999, 38 (9S), 5305.

28. Torrance, J. B.; Lacorre, P.; Nazzal, A. I.; Ansaldo, E. J.; Niedermayer, C., Systematic study of insulator-metal transitions in perovskites $RNiO_3$ (R=Pr,Nd,Sm,Eu) due to closing of charge-transfer gap. Physical Review B 1992, 45 (14), 8209-8212.

29. Raveau, B.; Maignan, A.; Martin, C., Insulator–Metal Transition Induced by Cr and Co Doping in $Pr_{0.5}Ca_{0.5}MnO_3$. Journal of Solid State Chemistry 1997, 130 (1), 162-166.

30. Qi, T.; Grinberg, I.; Rappe, A. M., Correlations between tetragonality, polarization, and ionic displacement in $PbTiO_3$-derived ferroelectric perovskite solid solutions. Physical Review B 2010, 82 (13), 134113.

31. Li, J.; Subramanian, M. A.; Rosenfeld, H. D.; Jones, C. Y.; Toby, B. H.; Sleight, A. W., Clues to the Giant Dielectric Constant of $CaCu_3Ti_4O_{12}$ in the Defect Structure of "$SrCu_3Ti_4O_{12}$". Chemistry of Materials 2004, 16 (25), 5223-5225.

32. Subramanian, M. A.; Li, D.; Duan, N.; Reisner, B. A.; Sleight, A. W., High Dielectric Constant in $ACu_3Ti_4O_{12}$ and $ACu_3Ti_3FeO_{12}$ Phases. Journal of Solid State Chemistry 2000, 151 (2), 323-325.

33. Ramirez, A. P.; Subramanian, M. A.; Gardel, M.; Blumberg, G.; Li, D.; Vogt, T.; Shapiro, S. M., Giant dielectric constant response in a copper-titanate. Solid State Communications 2000, 115 (5), 217-220.

34. Homes, C. C.; Vogt, T.; Shapiro, S. M.; Wakimoto, S.; Ramirez, A. P., Optical Response of High-Dielectric-Constant Perovskite-Related Oxide. Science 2001, 293 (5530), 673-676.

35. Sánchez-Benítez, J.; Alonso, J. A.; de Andrés, A.; Martínez-Lope, M. J.; Casais, M. T.; Martínez, J. L., Improving room temperature magnetoresistance in derivatives of ferrimagnetic $CaCu_3Mn_4O_{12}$ perovskite. Journal of Magnetism and Magnetic Materials 2004, 272-276, 1407-1409.

36. Weht, R.; Pickett, W. E., Magnetoelectronic properties of a ferrimagnetic semiconductor: The hybrid cupromanganite $CaCu_3Mn_4O_{12}$. Physical Review B 2001, 65 (1), 014415.

37. Howard, C. J., Stokes, H. T., , Group-Theoretical Analysis of Octahedral Tilting in Perovskites. Acta Crystallographica Section B 1998, 54 (6), 0108-7681.

38. Kushima, A.; Parfitt, D.; Chroneos, A.; Yildiz, B.; Kilner, J. A.; Grimes, R. W., Interstitialcy diffusion of oxygen in tetragonal $La_2CoO_{4+\delta}$. Physical Chemistry Chemical Physics 2011, 13 (6), 2242-2249.

39. Zhang, J., PEM fuel cell electrocatalysts and catalyst layers: fundamentals and applications. Springer Science & Business Media: 2008.

40. Riess, I., Mixed ionic–electronic conductors—material properties and applications. Solid State Ionics 2003, 157 (1), 1-17.

41. Jung, W.; Tuller, H. L., Impedance study of $SrTi_{1-x}Fe_xO_{3-\delta}$ (x=0.05 to 0.80) mixed ionic-electronic conducting model cathode. Solid State Ionics 2009, 180 (11), 843-847.

42. Orlovskaya, N.; Browning, N., Mixed ionic electronic conducting perovskites for advanced energy Systems. Springer Science & Business Media: 2012; Vol. 173.

43. Adler, S. B.; Lane, J. A.; Steele, B. C. H., Electrode kinetics of porous mixed-conducting oxygen electrodes. Journal of the Electrochemical Society 1996, 143 (11), 3554-3564.

44. Richter, J.; Holtappels, P.; Graule, T.; Nakamura, T.; Gauckler, L. J., Materials design for perovskite SOFC cathodes. Monatshefte für Chemie-Chemical Monthly 2009, 140 (9), 985-999.

45. Singhal, S. C.; Eguchi, K., Solid Oxide Fuel Cells 12 (SOFC-XII). Electrochemical Society: 2011.

46. Rodriguez-Carvajal, J.; Fernandez-Diaz, M. T.; Martinez, J. L., Neutron diffraction study on structural and magnetic properties of La_2NiO_4. Journal of Physics: Condensed Matter 1991, 3 (19), 3215.

47. Liu, X.; Hong, R.; Tian, C., Tolerance factor and the stability discussion of ABO_3-type ilmenite. Journal of Materials Science: Materials in Electronics 2009, 20 (4), 323-327.

48. Tomkiewicz, A. C.; Tamimi, M.; Huq, A.; McIntosh, S., Oxygen transport pathways in Ruddlesden–Popper structured oxides revealed via in situ neutron diffraction. Journal of Materials Chemistry A 2015, 3 (43), 21864-21874.

49. Yakal-Kremski, K.; Mogni, L. V.; Montenegro-Hernández, A.; Caneiro, A.; Barnett, S. A., Determination of Electrode Oxygen Transport Kinetics Using Electrochemical Impedance Spectroscopy Combined with Three-Dimensional Microstructure Measurement: Application to $Nd_2NiO_{4+\delta}$. Journal of The Electrochemical Society 2014, 161 (14), 1366-1374.

50. Islam, M. S., Ionic transport in ABO_3 perovskite oxides: a computer modelling tour. Journal of Materials Chemistry 2000, 10 (4), 1027-1038.

51. Ishigaki, T.; Yamauchi, S.; Kishio, K.; Mizusaki, J.; Fueki, K., Diffusion of oxide ion vacancies in perovskite-type oxides. Journal of Solid State Chemistry 1988, 73 (1), 179-187.

52. Carter, S.; Selcuk, A.; Chater, R. J.; Kajda, J.; Kilner, J. A.; Steele, B. C. H., Oxygen transport in selected nonstoichiometric perovskite-structure oxides. Solid State Ionics 1992, 53, 597-605.

53. Burriel, M.; Garcia, G.; Santiso, J.; Kilner, J. A.; Chater, R. J.; Skinner, S. J., Anisotropic oxygen diffusion properties in epitaxial thin films of $La_2NiO_{4+\delta}$. Journal of materials chemistry 2008, 18 (4), 416-422.

54. Skinner, S. J.; Kilner, J. A., Oxygen diffusion and surface exchange in $La_{2-x}Sr_xNiO_{4+\delta}$. Solid State Ionics 2000, 135 (1), 709-712.

55. Perez-Mato, J. M.; Orobengoa, D.; Aroyo, M. I., Mode crystallography of distorted structures. Acta Crystallographica Section A: Foundations of Crystallography 2010, 66 (5), 558-590.

56. Stokes, H. T.; Hatch, D. M.; Wells, J. D., Group-theoretical methods for obtaining distortions in crystals: Applications to vibrational modes and phase transitions. Physical Review B 1991, 43 (13), 11010.

57. Hatch, D. M.; Stokes, H. T., Complete listing of order parameters for a crystalline phase transition: A solution to the generalized inverse Landau problem. Physical Review B 2001, 65 (1), 014113.

58. Kresse, G.; Furthmüller, J., Efficient iterative schemes for \textit{ab initio} total-energy calculations using a plane-wave basis set. Physical Review B 1996, 54 (16), 11169-11186.

59. Kresse, G.; Joubert, D., From ultrasoft pseudopotentials to the projector augmented-wave method. Physical Review B 1999, 59 (3), 1758-1775.

60. Blöchl, P. E., Projector augmented-wave method. Physical Review B 1994, 50 (24), 17953.

61. Henkelman, G.; Uberuaga, B. P.; Jónsson, H., A climbing image nudged elastic band method for finding saddle points and minimum energy paths. The Journal of chemical physics 2000, 113 (22), 9901-9904.

62. Lee, Y.-L.; Kleis, J.; Rossmeisl, J.; Morgan, D., Ab initio energetics of $LaBO_3$ (001)(B= Mn, Fe, Co, and Ni) for solid oxide fuel cell cathodes. Physical Review B 2009, 80 (22), 224101.

63. Chroneos, A.; Parfitt, D.; Kilner, J. A.; Grimes, R. W., Anisotropic oxygen diffusion in tetragonal $La_2NiO_{4+\delta}$: molecular dynamics calculations. Journal of Materials Chemistry 2010, 20 (2), 266-270.

64. Frank, W.; Elsässer, C.; Fähnle, M., \textit{Ab initio} Force-Constant Method for Phonon Dispersions in Alkali Metals. Physical Review Letters 1995, 74 (10), 1791-1794.

65. May, S. J.; Kim, J. W.; Rondinelli, J. M.; Karapetrova, E.; Spaldin, N. A.; Bhattacharya, A.; Ryan, P. J., Quantifying octahedral rotations in strained perovskite oxide films. Physical Review B 2010, 82 (1), 014110.

66. Hatt, A. J.; Spaldin, N. A., Structural phases of strained $LaAlO_3$ driven by octahedral tilt instabilities. Physical Review B 2010, 82 (19), 195402.

67. Yamada, H.; Kawasaki, M.; Tokura, Y., Epitaxial growth and valence control of strained perovskite $SrFeO_3$ films. Applied physics letters 2002, 80, 622.

68. Yashima, M.; Sirikanda, N.; Ishihara, T., Crystal structure, diffusion path, and oxygen permeability of a Pr_2NiO_4-based mixed conductor $(Pr_{0.9}La_{0.1})_2(Ni_{0.74}Cu_{0.21}Ga_{0.05})O_{4+\delta}$. Journal of the American Chemical Society 2010, 132 (7), 2385-2392.

69. Yashima, M.; Tsuji, T., Structural investigation of the cubic perovskite-type doped lanthanum cobaltite $La_{0.6}Sr_{0.4}CoO_{3-\delta}$ at 1531 K: possible diffusion path of oxygen ions in an electrode material. Journal of Applied Crystallography 2007, 40 (6), 1166-1168.

70. Cherry, M.; Islam, M. S.; Catlow, C. R. A., Oxygen Ion Migration in Perovskite-Type Oxides. Journal of Solid State Chemistry 1995, 118 (1), 125-132.

71. Hoang, K.; Johannes, M. D., Defect chemistry in layered transition-metal oxides from screened hybrid density functional calculations. Journal of Materials Chemistry A 2014, 2 (15), 5224-5235.

72. Bassat, J.-M.; Odier, P.; Villesuzanne, A.; Marin, C.; Pouchard, M., Anisotropic ionic transport properties in $La_2NiO_{4+\delta}$ single crystals. Solid State Ionics 2004, 167 (3), 341-347.

73. Bassat, J.-M.; Burriel, M. n.; Wahyudi, O.; Castaing, R. m.; Ceretti, M.; Veber, P.; Weill, I.; Villesuzanne, A.; Grenier, J.-C.; Paulus, W., Anisotropic oxygen diffusion properties in $Pr_2NiO_{4+\delta}$ and $Nd_2NiO_{4+\delta}$ single crystals. The Journal of Physical Chemistry C 2013, 117 (50), 26466-26472.

74. Benedek, N. A.; Fennie, C. J., Why Are There So Few Perovskite Ferroelectrics? The Journal of Physical Chemistry C 2013, 117 (26), 13339-13349.

75. Woodward, P., Octahedral Tilting in Perovskites. II. Structure Stabilizing Forces. Acta Crystallographica Section B 1997; Vol. 53, p 44-66.

76. Mulder, A. T.; Benedek, N. A.; Rondinelli, J. M.; Fennie, C. J., Turning ABO_3 Antiferroelectrics into Ferroelectrics: Design Rules for Practical Rotation-Driven Ferroelectricity in Double Perovskites and $A_3B_2O_7$ Ruddlesden-Popper Compounds. Advanced Functional Materials 2013, 23 (38), 4810-4820.

77. Fukushima, T.; Stroppa, A.; Picozzi, S.; Perez-Mato, J. M., Large ferroelectric polarization in the new double perovskite $NaLaMnWO_6$ induced by non-polar instabilities. Physical Chemistry Chemical Physics 2011, 13 (26), 12186-12190.

78. Aimi, A.; Mori, D.; Hiraki, K.-i.; Takahashi, T.; Shan, Y. J.; Shirako, Y.; Zhou, J.; Inaguma, Y., High-Pressure Synthesis of A-Site Ordered Double Perovskite $CaMnTi_2O_6$ and Ferroelectricity Driven by Coupling of A-Site Ordering and the Second-Order Jahn–Teller Effect. Chemistry of Materials 2014, 26 (8), 2601-2608.

79. Li, Z.; Cho, Y.; Li, X.; Li, X.; Aimi, A.; Inaguma, Y.; Alonso, J. A.; Fernandez-Diaz, M. T.; Yan, J.; Downer, M. C.; Henkelman, G.; Goodenough, J. B.; Zhou, J., New Mechanism for Ferroelectricity in the Perovskite $Ca_{2-x}Mn_xTi_2O_6$ Synthesized

by Spark Plasma Sintering. Journal of the American Chemical Society 2018, 140 (6), 2214-2220.

80. Yang, C. N., The Spontaneous Magnetization of a Two-Dimensional Ising Model. Physical Review 1952, 85 (5), 808-816.

81. Talapov, A. L.; Blöte, H. W. J., The magnetization of the 3D Ising model. Journal of Physics A: Mathematical and General 1996, 29 (17), 5727.

82. Voter, A. F. In INTRODUCTION TO THE KINETIC MONTE CARLO METHOD, Radiation Effects in Solids, Dordrecht, 2007; Sickafus, K. E.; Kotomin, E. A.; Uberuaga, B. P., Eds. Springer Netherlands: Dordrecht, 2007; 1-23.

83. Cheng, J. G.; Zhou, J. S.; Goodenough, J. B., Thermal conductivity, electron transport, and magnetic properties of single-crystal $Ca_3Co_2O_6$. Physical Review B 2009, 79 (18), 184414.

84. Anderson, O. L.; Soga, N., A restriction to the law of corresponding states. Journal of Geophysical Research 1967, 72 (22), 5754-5757.

85. Anderson, O. L.; Nafe, J. E., The bulk modulus-volume relationship for oxide compounds and related geophysical problems. Journal of Geophysical Research 1965, 70 (16), 3951-3963.

86. Ozaki, Y., Ghedira, M.,Chenavas, J.,Joubert, J. C.,Marezio, M., , High-pressure synthesis and bond lengths of calcium copper germanium oxide $[CaCu_3](Ge_4)O_{12}$. Acta Crystallographica Section B 1977, 33 (11), 0567-7408.

87. Subramanian, M. A.; Marshall, W. J.; Calvarese, T. G.; Sleight, A. W., Valence degeneracy in $CaCu_3Cr_4O_{12}$. Journal of Physics and Chemistry of Solids 2003, 64 (9), 1569-1571.

88. Zeng, Z.; Greenblatt, M.; Subramanian, M. A.; Croft, M., Large Low-Field Magnetoresistance in Perovskite-type $CaCu_3Mn_4O_{12}$ without Double Exchange. Physical Review Letters 1999, 82 (15), 3164-3167.

89. Krimmel, A.; Günther, A.; Kraetschmer, W.; Dekinger, H.; Büttgen, N.; Loidl, A.; Ebbinghaus, S. G.; Scheidt, E. W.; Scherer, W., Non-Fermi-liquid behavior in $CaCu_3Ru_4O_{12}$. Physical Review B 2008, 78 (16), 165126.

90. Xin, Y.; Zhou, H. D.; Cheng, J. G.; Zhou, J. S.; Goodenough, J. B., Study of atomic structure and electronic structure of an $AA'_3B_4O_{12}$ double-perovskite $CaCu_3Ir_4O_{12}$ using STEM imaging and EELS techniques. Ultramicroscopy 2013, 127, 94-99.

91. Birch, F., Finite Elastic Strain of Cubic Crystals. Physical Review 1947, 71 (11), 809-824.

92. Murnaghan, F. D., The Compressibility of Media under Extreme Pressures. Proceedings of the National Academy of Sciences of the United States of America 1944, 30 (9), 244-247.

93. Cynn, H.; Klepeis, J. E.; Yoo, C.-S.; Young, D. A., Osmium has the Lowest Experimentally Determined Compressibility. Physical Review Letters 2002, 88 (13), 135701.

94. McSkimin, H. J.; Jr., P. A., Elastic Moduli of Diamond as a Function of Pressure and Temperature. Journal of Applied Physics 1972, 43 (7), 2944-2948.

95. Gillet, P.; Fiquet, G.; Daniel, I.; Reynard, B.; Hanfland, M., Equations of state of ^{12}C and ^{13}C diamond. Physical Review B 1999, 60 (21), 14660-14664.

96. Yu, R.; Zhang, X. F., Family of noble metal nitrides: First principles calculations of the elastic stability. Physical Review B 2005, 72 (5), 054103.